Icarus 369 (2021) 114634

Contents lists available at ScienceDirect

Icarus

journal homepage: www.elsevier.com/locate/icarus

Simultaneous sublimation activity of primitive asteroids including (24) Themis and (449) Hamburga: Spectral signs of an exosphere and the solar activity impact

Vladimir V. Busarev [a,b,*], Elena V. Petrova [c], Tatiana R. Irsmambetova [a], Marina P. Shcherbina [a], Sergey I. Barabanov [b]

[a] Lomonosov Moscow State University, Sternberg Astronomical Institute (SAI MSU), University Av., 13, 119992 Moscow, Russia
[b] Institute of Astronomy, Russian Academy of Sciences (IA RAS), Pyatnitskaya St. 48, 109017 Moscow, Russia
[c] Space Research Institute, Russian Academy of Sciences, Profsoyuznaya 84/32, Moscow 117997, Russia

ARTICLE INFO

Keywords:
Asteroids
Spectrophotometry
Ices
Radiative transfer
Solar wind

ABSTRACT

We describe and analyze simultaneous sublimation activity of the main-belt primitive asteroids during their perihelion passages, which was detected by spectral methods. This phenomenon was observed for the first time in September 2012 for asteroids (145) Adeona, (704) Interamnia, (779) Nina, and Mars-crosser (1474) Beira (Busarev et al., 2015, 2016, 2018, 2019a). By our recent observations of (704) Interamnia, (24) Themis, and (449) Hamburga performed in March–April 2019, we confirmed the existence of this effect. (24) Themis and (449) Hamburga was detected as active for the first time. Never before, two or more asteroids have been observed active simultaneously. Activity on asteroids reveals itself by unusual spectral features (the maxima at approximately 0.40–0.50 and/or 0.60–0.70 μm), which appear in the reflectance spectra of the bodies when they approach perihelion. We explain them as manifestations of sublimation of ice materials and development of a subtle exosphere around the asteroids. Moreover, from numerical simulations of the light scattering in a medium containing ice and silicate/organic dust particles of complex structure, we found that some of these models fit well the reflectance spectra of active asteroids, which confirms the presence of a rarefied exosphere around these bodies. Our results show that the main conditions providing formation of a temporal sublimation-driven exosphere around primitive main-belt asteroids are: (1) the considerably higher content of H_2O in their material than that previously believed from accounting for only the content of bound water in composition of carbonaceous chondrites, as possible components of asteroids; (2) frequent collisions of main-belt asteroids with smaller bodies and/or exposure to meteorite fluxes, which leads to excavation of ices and their subsequent sublimation; (3) the recurrent rise of the subsolar temperature on the surface of asteroids under proper orbital or dynamical parameters and the sublimation of subsurface ices (if present); and (4) the strengthening of solar activity (and the accompanying factors), which results in desiccation, destruction and/or dispersion of hydrated silicates and/or radiation damage of organic films isolating stocks of volatiles on or under the asteroid surface. According to our analysis, none of these factors produces a noticeable effect alone and can be marked as stronger or more frequent, but two or three of them working simultaneously may be effective.

1. Introduction

To date, about 30 objects moving along asteroid orbits in the Main asteroid belt (MAB) showed signs of cometary activity. To systematize the observational data from different sources as well as the mechanisms proposed to explain activity of the bodies, considerable efforts have been recently undertaken (e.g., Chandler et al., 2018, and references therein). The authors formulated the criteria, by which one could identify a particular mechanism of the bodies' activity (e.g., a perihelion passage and repetitive sublimation of ices at elevated subsolar temperatures, collisions of bodies, destruction of a body due to fast rotation, etc.). Among these cases, a rather rare one is activity of an ice-containing body at an arbitrary point of its orbit, which is caused by collision with another body; one of the examples is (596) Sheila (Jewitt, 2012). The

* Corresponding author at: Lomonosov Moscow State University, Sternberg Astronomical Institute (SAI MSU), University Av., 13, 119992 Moscow, Russia.
E-mail address: busarev@sai.msu.ru (V.V. Busarev).

https://doi.org/10.1016/j.icarus.2021.114634
Received 21 November 2020; Received in revised form 4 July 2021; Accepted 25 July 2021
Available online 28 July 2021

most pronounced signs of activity in such a small body are a temporary comet-like coma and a tail, which is a result of the mass loss and the sublimation of ice excavated from interiors of the asteroid. At first, these features provoked some authors to identify active asteroids in the MAB as "main-belt comets" (e.g., Hsieh and Jewitt, 2006; Hsieh and Haghighipour, 2016). At the same time, a thorough analysis of the observational data on a dozen of active main-belt asteroids suggested that their activity may be induced by some other factors, such as electrostatic repulsion, radiation pressure sweeping, dehydration stresses, and thermal fracture, or their combinations in addition to sublimation of ice (Jewitt, 2012). Thus, the activity events on asteroids may be more complex and not yet fully understood. Interestingly, the recent results led some investigators to conclusion that ices could be widespread in interiors of asteroids in the outer part of the MAB (e.g., Jewitt et al., 2015).

The suggestion about the presence of a considerable number of alien comet nuclei in the MAB inevitably faces the problem of celestial mechanics concerning regular transformation of cometary orbits into asteroid ones. However, the events of activity on the MAB asteroids may easily be explained, if we assume that asteroids of primitive types (C, B, G, F, D, and P) originally contained much more water ice. If the content of bound water in carbonaceous chondrites (as probable components of such asteroids) reaches ~20 wt% (e.g., Dodd, 1981; Jarosewich, 1990; Alexander et al., 2018), the content of unbound H_2O in the material of primitive-type asteroids may not be less. Thus, the problem of activity in asteroids may be solved, if the material of main-belt primitive asteroids originally contained much more H_2O than that in carbonaceous chondrites in terrestrial collections. Obviously, this important issue is closely connected with another one – the possibility of delivering water ice by small bodies to the Earth and other terrestrial planets.

For the first time, the spectral signs of simultaneous sublimation activity (the unusual maxima at approximately 0.40–0.50 and/or 0.60–0.70 μm) on primitive-type asteroids were established in September 2012 (Busarev et al., 2015, 2016, 2018, 2019a). At that time, these asteroids—(145) Adeona, (704) Interamnia, and (779) Nina, which are members of the MAB, and (1474) Beira, which is a Mars-crosser—were close to their perihelia. Together with the mentioned active asteroids (145, 704, 779 and 1474), spectrophotometry of (32) Pomona and two Near Earth Asteroids (NEAs) - (330825) 2008 XE3 and (2012 QG42) was carried out in a period of September 12 to 20, 2012 (Busarev et al., 2015, 2016). Similar spectral effects, although of lesser intensity, were repeatedly observed for Adeona, Interamnia, and Nina during their next perihelion passages in 2016–2018 (Busarev et al., 2018, 2019a). By now, due to unfavorable observational conditions at the Terskol observatory, no chance has appeared to observe Beira at its next perihelion passage (Busarev et al., 2015). Because of this, to study activity of this extremely interesting asteroid in more detail, we urge other observers around the world to measurer its spectra near the perihelion in years ahead.

However, similar spectral signs of simultaneous sublimation activity were observed on three primitive asteroids - (24) Themis, (449) Hamburga, and (704) Interamnia - in March 2019 (Busarev et al., 2019b). We explained this result by considerable orbital eccentricities of the bodies and the influence of general cosmogonic and evolutionary factors to them, which may create conditions for ices (mainly H_2O ice) to sublimate from the surface at elevated subsolar temperatures, which, in turn, leads to forming a temporary exosphere. By the moment, there are reliable findings of an exosphere permanently existing around at least two minor bodies – (1) Ceres (s) and (2060) Chiron (Küppers et al., 2014; Meech and Belton, 1990). In the first case, the exosphere was directly detected by several space-born methods, while in the second one, its presence follows from the results of reliable model simulations.

In this paper, we review the observations of simultaneous sublimation activity of asteroids manifested in their reflectance spectra and attempt to explain some differences in their spectral behavior. To confirm the presence of asteroid exosphere as a reason of the unusual observed spectral features, we numerically model the reflectance spectra of asteroids enveloped by a thin exosphere, for which the theory of light scattering by agglomerates of submicron particles is used. We take into account their chemical and mineralogical composition (by means of the refractive index), structure, and sizes, as well as the spectral characteristics of the asteroid surface and the optical thickness of a presumed exosphere. Additionally, during the period of low solar activity (the spring of 2019), we succeeded in registering and identifying for the first time a direct impact of solar flares (and associated events such as coronal mass ejections) on the reflectance spectra of active asteroids under consideration (24, 449, and 704). It is worth noting that the influence of the solar wind on the activity events in comet 67P/Churyumov-Gerasimenko depending on its heliocentric distance was established (Nilsson et al., 2015). Moreover, according to Geostationary Operational Environmental Satellite (GOES) data, the impact of solar X-ray flares on the heliocentric distribution of cometary flares of some Jupiter-family and main-belt comets changes with their heliocentric longitude and distance (though, no direct correlation between the solar activity variations and cometary flares was found) (Musiichuk and Borysenko, 2019). However, since these effects on small bodies are complex and unpredictable, their indication remains quite a rare event.

2. Spectral signs of sublimation activity of asteroids and a possible impact of solar activity

2.1. Unusual features in the spectra of (145) Adeona, (704) Interamnia, (779) Nina, and (1474) Beira

The important physical and dynamical parameters of these asteroids are as follows. Adeona is 127.783 km on average across (Masiero et al., 2014); its rotational period is 15.071^h (Warner et al., 2009), and the orbital period and the eccentricity are 4.37 yr and $e = 0.1453$, respectively (http://ssd.jpl.nasa.gov/sbdb.cgi#top). Interamnia is an asteroid 306.313 km across (Masiero et al., 2014) rotating with a period of 8.727^h (Warner et al., 2009) and orbiting the Sun with a period of 5.34 yr and an eccentricity of $e = 0.1552$ (http://ssd.jpl.nasa.gov/sbdb.cgi#top). The average diameter of Nina is 80.57 km (Masiero et al., 2014), and it rotates with a period of 11.186^h (Warner et al., 2009) and orbits the Sun for 4.35 yr with an eccentricity of $e = 0.2278$ (http://ssd.jpl.nasa.gov/sbdb.cgi#top). The Mars-crosser Beira has a rotational period of 4.184^h (Warner et al., 2009) and orbits the Sun for 4.52 yr and with an eccentricity of $e = 0.4890$ (http://ssd.jpl.nasa.gov/sbdb.cgi#top). The diameter of Beira is estimated as ~10 km (Busarev et al., 2016).

According to the common classifications (Tholen, 1989; Bus and Binzel, 2002), Adeona is an asteroid of C or Ch type, Interamnia – of F or B type, Nina – of M or X type, and Beira – of FX or B type. The values of the geometric V-band albedo of Adeona, Interamnia, and Nina are 0.06, 0.08, and 0.16, respectively (Masiero et al., 2014). Taking into account the B classification of Beira (Bus and Binzel, 2002), we conditionally adopted its geometric albedo (still unknown) as ~0.08. It is important to note that asteroids of this type are supposed to be primitive, including low-temperature compounds (hydrated silicates, oxides, organics, etc.) (e.g., Gaffey et al., 1989, 2002). Despite the previously debated high-temperature mineralogy of Nina, radar observations showed that the asteroid may also be primitive but heterogeneous in composition (Shepard et al., 2010).

The above described asteroids are not the objects, the signs of activity of which have ever been searched for before. At the same time, (145) Adeona, (704) Interamnia, and (779) Nina were covered by the spectrophotometric Small Mainbelt Asteroid Spectroscopic Survey (SMASS) and SMASSII survey (https://sbnapps.psi.edu/ferret/).

It should be stressed that (145) Adeona is a member (and the largest one) of a numerous dynamical asteroid family consisting of more than 2200 small bodies (Nesvorný et al., 2015). So, Adeona is of interest as a probably survived parent body of this family.

The unusual maxima near 0.45–0.70 μm in the reflectance spectra of four main-belt primitive-type asteroids of different types, (145) Adeona, (704) Interamnia, (779) Nina, and (1474) Beira, were almost simultaneously registered for the first time in September 2012, when the bodies were close to their perihelia (Fig. 1) (Busarev et al., 2015, 2016). At that time, Adeona was the farthest one from the perihelion: sublimation activity of the asteroid could start about a year before its perihelion passage (or at a distance of about 0.4 AU from the perihelion). An additional comment about these details is given in the Section 2.4. Spectrophotometric observations of the asteroids and a nearby solar analog star (HD 10307) were performed with the 2-m telescope and a CCD-spectrograph (with a low spectral resolution $R \approx 100$) of the Terskol observatory of the Institute of Astronomy of Russian Academy of Science (RAS). The observations were performed under high-altitude conditions (at the altitude exceeding 3000 m above sea level). The raw data were processed according to a generally accepted method of the CCD-data processing. Besides, the reflectance spectra of discussed asteroids were calculated by a standard procedure of dividing the spectrum of an asteroid by the spectrum of the nearby solar analog star with accounting for the difference in their atmospheric air masses. The procedure makes it possible to exclude or reduce to a minimum the influence of the terrestrial atmosphere on the retrieved spectra. We used HD10307 as a solar analog, though its spectral continuum differs from that of the Sun: the discrepancy starts from a wavelength of ~600 nm and grows toward short wavelengths reaching ~10% at 350 nm (Hardorp, 1980). Thus, we estimate the maximal errors in our reflectance spectra at the short-wavelength boundary just by this magnitude. In general, the relative standard deviations of the measurements are within 3–10% near the blue and red boundaries of the spectral range (0.35–0.90 μm) and no more than 1.5% in the visible range.

It should also be emphasized that the discussed spectral effects of sublimation activity were not found on other three asteroids observed in September 2012 together with those mentioned above (Busarev et al., 2015, 2016). Observational parameters of the asteroids are shown in Table 1, and their averaged reflectance spectra for corresponding dates are presented in Fig. 1a–d together with their SMASSII reflectance spectra for comparison (in case of availability).

Similar features in the spectra of Adeona, Interamnia, and Nina, although less pronounced, were registered during their next perihelion passages in 2016–2018 (Busarev et al., 2018, 2019a). The reflectance spectra of Interamnia may serve as a typical example of weak spectral changes associated with the presence of a sublimation-driven exosphere (Busarev et al., 2019a). These spectra were obtained on June 23 and 27, 2017 at very close relative rotational phases, but their gradients are of different signs (see Fig. 2a and b). A reasonable explanation of the spectral features of Interamnia is that they are induced by the presence of a tenuous sublimation-driven exosphere and the changes, taking place in it at elevated subsolar temperatures. In our opinion, the difference between these spectral features and those of the asteroids observed in 2012 (unusual maxima near 0.45–0.55 μm) may be explained by different conditions in their exospheres during the observations (see the explanations in Sections 3.3 and 4).

The predominance of H_2O ice in the material of main-belt primitive asteroids (among other volatile compounds including CO_2 ice, which is close in characteristics to H_2O ice, but more volatile) follows from the correspondence of its thermo-physical parameters to the effective temperatures of these bodies on their heliocentric distances (e.g., Dodson-Robison et al., 2009; Philippe et al., 2015; Schorghofer, 2016; Poch

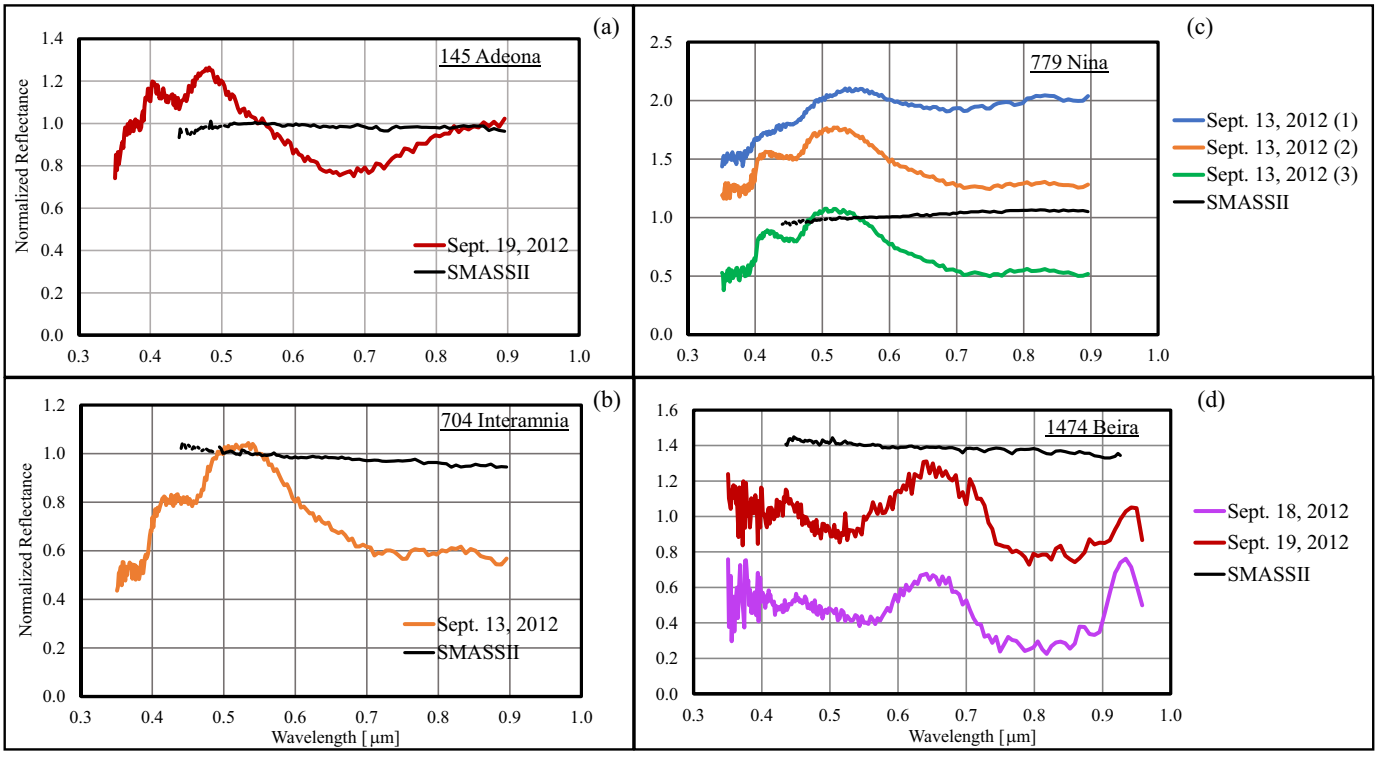

Fig. 1. The reflectance spectra of active primitive asteroids of the Main belt (normalized to the value at 0.55 μm) obtained in September 2012 (Busarev et al., 2015, 2016): (145) Adeona (a), (704) Interamnia (b), (779) Nina (c), and (1474) Beira (d). The averaged observational parameters of these asteroids are given in Table 1. Three spectra of (779) Nina and two spectra of (1474) Beira are shifted along the vertical axis for clarity. The SMASSII reflectance spectra of the asteroids are given for comparison (Lazzaro et al., 2006; https://sbnapps.psi.edu/ferret/).

Note: Hereafter, not to overload the diagrams, the errors of spectrophotometric measurements are given in the text.

Table 1
Averaged parameters of observations of asteroids (145) Adeona, (704) Interamnia, (779) Nina, and (1474) Beira in September 2012.

Date (y m d)	UT (h m s)	R.A. (h m)	Decl. (°)	Δ (AU)	*R* (AU)	*E* (°)	*Ph.* (°)	*V* (m)	Elev. (°)	Exp. time (s)	Air Mass	S/N
(145) Adeona (e = 0.1453, q = 2.2858 AU, D = 127.8 km, p_v = 0.06; C(Ch))												
2012 09 19	23 10 00	02 29.58	-01 38.1	1.843	2.692	140.1	13.9	12.4	44.0	1200	1.438	3.1
Solar analog star HD10307: Elev. 67°, UT = $01^h\ 32^m$, Air Mass 1.0862												
(704) Interamnia (e = 0.1552, q = 2.5817, D = 306.3 km, p_v = 0.08, F(B))												
2012 09 13	21 33 00	03 24.64	+39 00.3	2.080	2.616	111.1	21.0	10.9	51	600	1.2896	5
Solar analog star HD10307: Elev. 48°, UT = $19^h\ 25^m$, Air Mass 1.3446												
(779) Nina (e = 0.2278, q = 2.0577, D = 80.6 km, p_v = 0.16, M(X))												
2012 09 13	19 50 20	00 53.05	+32 41.0	1.289	2.149	138.6	18.0	11.0	55.2	300	1.3201	5.0
Solar analog star HD10307: Elev. 48°, UT = $19^h\ 25^m$, Air Mass 1.3446												
(1474) Beira (e = 0.4890, q = 1.3983, D ~ 10 km, p_v ~ 0.08, FX(B))												
2012 09 18	20 53 00	22 32.88	+32 60.4	0.651	1.567	141.4	23.6	13.8	73.3	1200	1.047	13.3
Solar analog star HD10307: Elev. 63°, UT = $01^h\ 30^m$, Air Mass 1.122												
2012 09 19	19 04 13	22 30.72	+33 24.3	0.649	1.563	140.8	24.0	13.8	72.7	1200	1.055	9.5
Solar analog star HD10307: Elev. 61°, UT = $01^h\ 30^m$, Air Mass 1.143												

Designations of quantities given in Tables 1 and 2: the universal time (UT) corresponding to the middle of the exposure time (Exp. time); the right ascension (R.A.); the declination (Decl.); the distance between the centers of the Earth and the object (Δ); the heliocentric distance (*R*) between the object and the Sun; the eccentricity of the orbit (*e*); the perihelion distance (*q*); the angular elongation of the object from the Sun (*E*); the phase angle of the object (*Ph.*); the visual magnitude of the object (*V*); the elevation of the object above the local horizon (Elev.); the atmospheric mass of the observed object (Air Mass); and the signal to noise ratio (S/N).

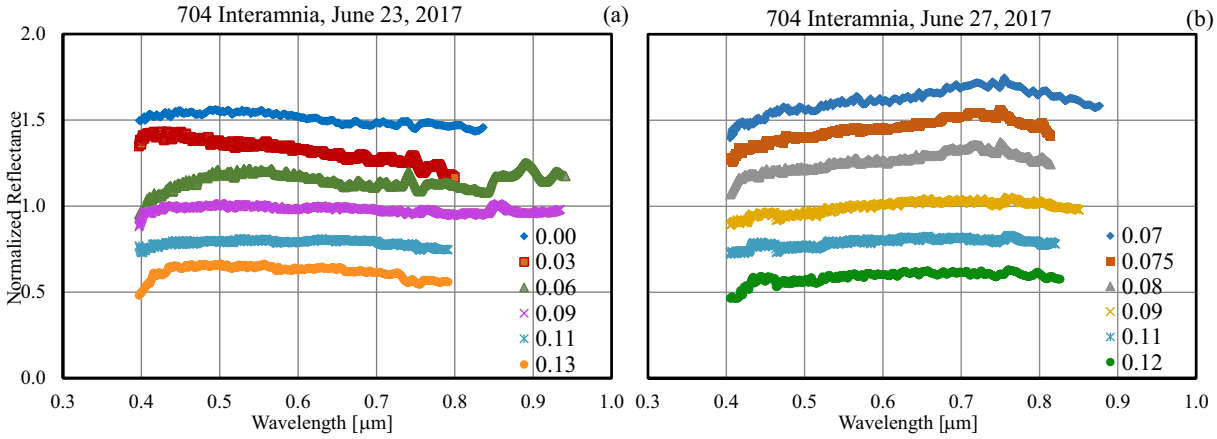

Fig. 2. Two sets of the reflectance spectra of (704) Interamnia approaching the perihelion, which were obtained on June 23 (a) and June 27 (b), 2017 at very close relative rotational phases (the corresponding values are given in the diagrams). The spectra are normalized to the value at 0.55 μm and shifted along the vertical axis for clarity. The overall gradient of the reflectance spectra of Interamnia on June 24 is negative, and that on June 27 is positive. The spectra demonstrate typical spectral changes associated with the presence of a tenuous sublimation-driven exosphere around the asteroid (Busarev et al., 2019a).

et al., 2016). On the other hand, the depletion of the asteroid surface with ice materials (the disappearance of CO_2 and the other most volatile compounds first of all) or their isolation (suffocation/quenching, e.g., if the ice particles become coated with organics) could stop replenishing the exosphere. Indeed, the formation of a lag deposit (or a sublimation mantle) made of a water-free porous network of organic filaments on top of the ice was confirmed in the modeling experiments with ice-tholins mixtures under low temperature (below −70 °C) and pressure (10^{-5} mbar) conditions (e.g., Philippe et al., 2015; Poch et al., 2016).

Besides, it is important to note that one of the most important conditions in the MAB is that ice materials on primitive asteroids are frequently excavated by repeated meteoroid impacts (e.g., Dermott et al., 1984; Durda and Dermott, 1997), which should create conditions for higher activity on asteroids of this kind, when the subsolar temperature grows near perihelion. However, the micrometeorite flux is poorly known. The values typical of the Moon, Mars, and outer objects are estimated in a range of 2×10^{-17} to 2×10^{-16} g cm^{-2} s^{-1} (Brunetto et al., 2015). The micrometeorite flux in the MAB has not been measured directly yet. The factor of thermal fracture exposing material could be as important as meteoroid impacts in the strengthening of sublimation activity of primitive asteroids, especially those with high eccentricities, like (3200) Phaethon (Jewitt and Li, 2010).

2.2. *Spectral signs of simultaneous sublimation activity of (24) Themis, (449) Hamburga, and (704) Interamnia in 2019*

Let consider the main parameters of (24) Themis and (449) Hamburga, which were detected as active asteroids for the first time in 2019. Themis is 198 km on average in diameter, which was determined by its geometric albedo of 0.067 according to the IRTF-measurements (https://ssd.jpl.nasa.gov/sbdb.cgi#top); its rotational period is 8.374^h (Warner et al., 2009), the orbital period is 5.55 yr, and the eccentricity is e = 0.1242 (http://ssd.jpl.nasa.gov/sbdb.cgi#top). Hamburga is an asteroid 85.59 km across (IRAS-A-FPA-3-RDR-IMPS-V6.0) rotating with a period of 36.516^h (Warner et al., 2009) and orbiting the Sun with a period of 4.08 yr and an eccentricity of e = 0.1722 (http://ssd.jpl.nasa.

gov/sbdb.cgi#top).

According to the common classifications, Themis is an asteroid of C (Tholen, 1989) or B (Bus and Binzel, 2002) type, while Hamburga is the C-type asteroid (EAR-A-5-DDR-TAXONOMY-V4.0). The geometric albedo of Hamburga is 0.04 (IRAS-A-FPA-3-RDR-IMPS-V6.0). The signs of activity have never been searched for on Themis and Hamburga; the first one was covered by the spectrophotometric SMASS and SMASSII surveys, while the second one, by the SDSS survey (https://sbnapps.psi.edu/ferret/).

Importantly, (24) Themis is the largest member of the Themis family located in the outer part of the MAB, at an average heliocentric distance of 3.13 AU; this is a family of approximately 540 asteroids of C-type, the composition of which is believed to be similar to that of carbonaceous chondrites (Nesvorný et al., 2015). As Adeona, Themis may be a survived parent body of its family.

Spectral signs of sublimation activity and impermanent exospheres were simultaneously detected in the reflectance spectra of main-belt primitive asteroids, having noticeable eccentricities of orbits—(24) Themis, (449) Hamburga, and (704) Interamnia (for Themis and Hamburga, for the first time)—on March 17–20 and April 10, 2019, when they were very close to perihelion (Busarev et al., 2019b) (Table 2). The approximate spectra were obtained from the multiband photometric data of the asteroids. The *UBVRI*-observations of Themis, Hamburga, and Interamnia along with a proper non-variable solar analog star, HIP 29759, were performed with the 0.6-m telescope at the Crimean observatory of the Sternberg Astronomical Institute of Lomonosov Moscow State University (SAI MSU). The telescope was equipped with a photometer and Apogee Aspen CCD matrix (2048 × 2048 pixels). The latter was used in the double binning mode, so the combined 2 × 2 pixel corresponds to 0.74″. The relative standard deviations of the measurements are within 2–3% in the *U* and *I* filters and no more than 1% in the other ones. The intensity of light reflected from these asteroids were registered in the effective wavelengths of the filters and converted to the reflectance by means of observations of the same solar analog star HIP 29759 (Table 2; see Busarev et al. (2019a, 2019b) for processing details). Figs. 3–5 present the normalized reflectance of Themis, Hamburga, and Interamnia measured at these dates in the (*U*)*BVRI*-filters. It was sometimes impossible to perform measurements in the *U*-filter due to restrictions in the observational time (the time was not sufficient to observe all of the necessary objects) or observational conditions (e.g., the altitudes of some objects were too low). Very similar spectral manifestations of a thin exosphere on all three asteroids—two maxima at 0.44 and 0.66 μm—are seen in the data for March 17 and 19. However, for some reason, these spectral features disappeared on the mid-point date, March 18. We interpret this strange phenomenon as sweeping away the asteroids' exosphere by a shockwave in the solar wind. We will discuss this issue at length in Section 2.4, but now let us consider how simultaneous sublimation activity of the considered asteroids is additionally confirmed by the results of photometry.

2.3. Photometric confirmations of simultaneous sublimation activity of (24) Themis, (449) Hamburga, and (704) Interamnia in 2019

Any visible signs of a coma or a tail in the images of Themis, Hamburga, and Interamnia obtained in March–April 2019 were not found during the observations probably due to a very low level of sublimation activity on the asteroids. The direct imaging of a main-belt active asteroid does not allow us to detect these signs of activity even with large ground-based telescopes under perfect photometric conditions, unless the size of a coma or a tail near the body exceeds a few hundred kilometers, which corresponds to 0.014–0.007″ for an observer on the Earth being at distances of 1–2 AU. Because of this, we attempted to find some additional signs of activity on the asteroids from the wide-band photometry data obtained, specifically, in the *V* band.

As it turned out, the apparent *V*-magnitudes of Themis, Hamburga, and Interamnia, which were computed from the observational data of March–April 2019 with the MaximDL program by using the nearby standard stars (from the NOMAD catalog (Zacharias et al., 2004)) seen in the same CCD-frames, were systematically lower than the ephemeris (model) magnitudes of the asteroids at the same wavelengths according to the IAU MPC (https://minorplanetcenter.net//iau/MPEph/MPEph.html) and JPL (https://ssd.jpl.nasa.gov/?asteroids) on-line services (Fig. 7, Table 2). As was discussed in our previous paper (Busarev et al., 2019a), the presence of an exosphere scattering light around an asteroid

Table 2
Parameters of observations of (24) Themis, (449) Hamburga, and (704) Interamnia in.

Date (y m d)	UT (h m s)	R.A. (h m s)	Decl. (° ′ ″)	Δ (AU)	*R* (AU)	*E* (°)	*Ph.* (°)	V_{mod} (^{m})	V_{meas} (^{m})	Air mass	St. Star	St. Star's air mass
(24) Themis (e = 0.1242, q = 2.7465 AU, D = 198 km; p_v = 0.067; C(B))												
2019 03 17	18 12 30	07 17 39	+23 10 27	2.235	2.756	111.2	19.7	12.148	11.29	1.093	HIP 29759	1.023
2019 03 18	18 04 49	07 18 04	+23 09 22	2.247	2.756	110.3	19.8	12.163	10.80	1.090	HIP 29759	1.076
2019 03 19	18 09 51	07 18 30	+23 08 14	2.260	2.755	109.4	19.9	12.178	11.30	1.097	HIP 29759	1.096
2019 03 20	18 03 05	07 18 58	+23 07 03	2.272	2.755	108.5	20.0	12.193	11.29	1.094	HIP 29759	1.093
2019 04 10	19 30 09	07 33 54	+22 30 11	2.539	2.750	91.2	21.4	12.470	11.73	1.473	HIP 29759	1.668
(449) Hamburga (e = 0.1722, q = 2.1107 AU; D = 85.6 km; p_v = 0.039; C)												
2019 03 17	17 41 45	07 48 59	+24 44 07	1.454	2.112	118.0	24.6	13.417	12.86	1.065	HIP 29759	1.023
2019 03 18	17 34 01	07 49 34	+24 42 09	1.464	2.112	117.1	24.8	13.438	12.76	1.066	HIP 29759	1.076
2019 03 19	17 30 08	07 50 11	+24 40 05	1.474	2.112	116.3	25.0	13.459	12.65	1.066	HIP 29759	1.096
2019 03 20	17 23 05	07 50 49	+24 37 55	1.484	2.113	115.4	25.2	13.480	12.9	1.068	HIP 29759	1.093
2019 04 10	19 47 22	08 10 43	+23 29 18	1.713	2.120	99.3	27.8	13.877	13.5	1.372	HIP 29759	1.6684
(704) Interamnia (e = 0.1552, q = 2.5817 AU; D = 306.3 km; p_v = 0.078; F(B))												
2019 03 17	18 32 19	07 10 47	+13 41 10	2.666	3.155	110.5	17.2	11.9	10.90	1.221	HIP 29759	1.023
2019 03 18	18 34 04	07 11 01	+13 40 06	2.680	3.157	109.6	17.3	11.9	10.82	1.230	HIP 29759	1.076
2019 03 19	18 45 47	07 11 17	+13 39 00	2.695	3.158	108.7	17.4	12.0	10.90	1.258	HIP 29759	1.096
2019 03 20	18 38 55	07 11 33	+13 37 55	2.710	3.159	107.8	17.5	12.0	10.95	1.252	HIP 29759	1.093
2019 04 10	19 16 28	07 21 43	+13 09 53	3.032	3.189	89.8	18.3	12.3	11.47	1.677	HIP 29759	1.668

March–April 2019.

Notes: (1) Standard exposure times for the asteroids were 300–360 and 120–200 s in filters *U* and *B*, respectively, and 30–90 s in the other ones. (2) V_{mod} – calculated visual magnitude of the object (according to https://ssd.jpl.nasa.gov/horizons.cgi); V_{meas} – visual magnitude of the object determined from the observational data (with MaximDL program). (3) Ephemerides of the asteroids including modeled visual magnitudes were obtained with the IAU MPC Ephemeris (https://minorplanetcenter.net//iau/MPEph/MPEph.html) and JPL on-line services (Giorgini et al., 1996). Eccentricity (*e*), perihelion (*q*), diameter (D), geometric albedo (p_v), and Tholen (and SMASSII, if available) spectral type of the asteroids are given according to JPL database (https://ssd.jpl.nasa.gov/sbdb.cgi#top).

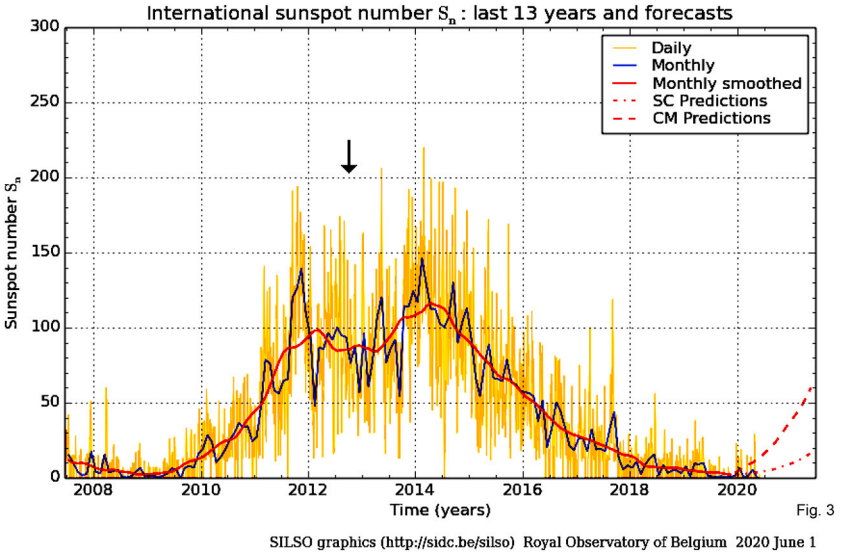

Fig. 3. The international sunspot number S_n for the last 13 years and forecasts from the Royal Observatory of Belgium on June 1, 2020 (http://sidc.be/silso). The time of our observations of (145) Adeona, (704) Interamnia, (779) Nina, and (1474) Beira in September 2012 is shown by a vertical arrow.

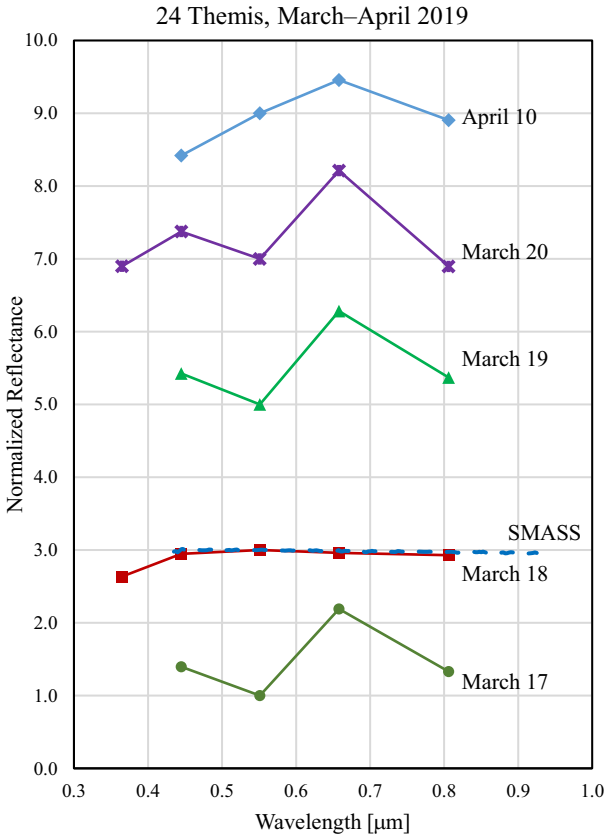

Fig. 4. The reflectance spectra of (24) Themis obtained from the *UBVRI* photometric data for March 17–20 and April 10, 2019, when the asteroid was very close to perihelion (Busarev et al., 2019b) (Table 2). The spectra are normalized to the value at 0.55 μm and shifted along the vertical axis for clarity. The spectrum measured on March 18 without maxima at 0.45 and 0.66 μm is compared with the "canonical" one of Themis from the SMASS database (Bus and Binzel, 2003; https://sbnapps.psi.edu/ferret/).

Note: Hereafter, not to overload the diagrams, the errors of spectrophotometric measurements are given in the text.

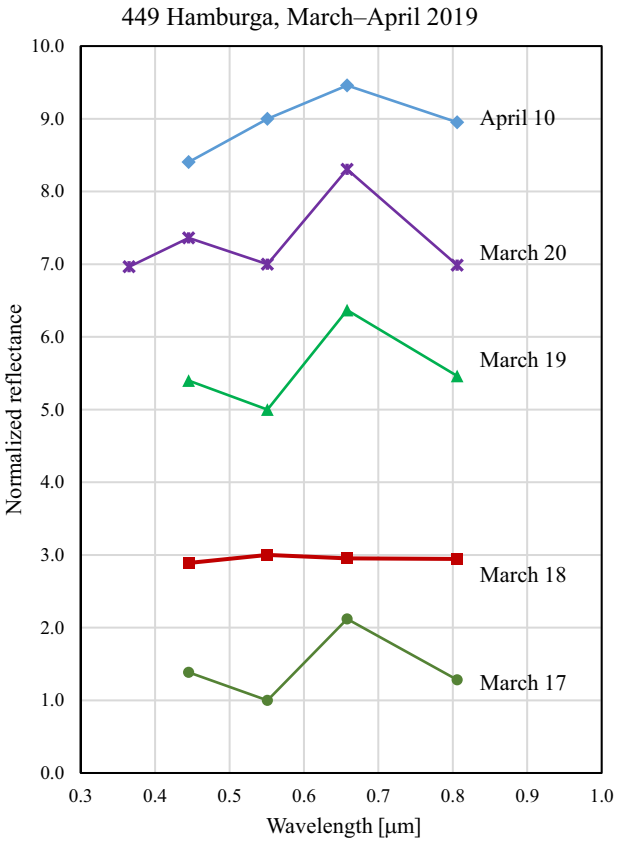

Fig. 5. The reflectance spectra of (449) Hamburga obtained from the observational *UBVRI*-data on March 17–20 and April 10, 2019, when the asteroid was very close to perihelion (Busarev et al., 2019b) (Table 2). The spectra are normalized to the value at 0.55 μm and shifted along the vertical axis for clarity.

makes it brighter and its stellar magnitude lower. Thus we consider this difference as a main additional confirmation of simultaneous sublimation activity of these bodies in March–April 2019.

The seeing conditions at the time of our *UBVRI*-observations with 0.6-m telescope of SAI MSU on 2019 March 17–19 and April 10 were near 0.74″ per CCD pixel and somewhat worse on March 20. All of the observations were performed in the double binning mode. The estimated full width of half-maximum (FWHM) of point-like images was around 2–3 pixel. To search for differences between the images of an asteroid and a star, we compared the mean brightness radial profiles of the asteroids with that of the nearby solar analog star, HIP 29759. The brightness radial profiles of Themis, Hamburga, and Interamnia (Fig. 8, orange curves) were determined by means of averaging their measured photometric profiles in several directions (horizontal, vertical, and diagonal) after subtracting the background signal and normalizing the curves. We assumed that the asteroids' exospheres were in a relatively stable state on March 17, before the action of a solar wind shock wave (see the discussion below). Given the size of the asteroid's image equal to two pixels, the inner aperture with an angular radius $\varphi_1 = 0.74''$ would sample the asteroid itself through a layer of the exosphere, while the annulus between φ_1 and an outer aperture of radius φ_2 (determined by the extent of the asteroid's radial profile exceeding that of the star) would provide a measure of the asteroid exosphere. Thus, the limiting numbers of pixels from the aperture center, corresponding to the outer aperture of radius φ_2 and determined on March 17 by the intersections of the radial brightness profile of the asteroid (orange) with that of HIP 29759 (blue), were 4, 4, and 3 for Themis, Hamburga, and Interamnia, respectively (Fig. 8). Also, the apparent magnitudes of the asteroids were calculated within the specified angular apertures on 2019 March 18–20 and April 10 (Table 2). According to our analysis, the largest excess of the radial profiles of the asteroids over that of HIP 29759 was on March 18 for Themis, and Interamnia and on March 19 for Hamburga, which meets the lowest apparent magnitudes of the asteroids at the time of the supposed impact produced by a shock wave of the solar wind (Fig. 7).

To estimate the mass losses caused by sublimation of ice from the asteroids, we tried to apply some methods developed for studying comets and active bodies in the MAB (e.g., A'Hearn et al., 1984; Meech et al., 1986; Jewitt, 2009, 2012; Shi and Ma, 2015; Chandler et al., 2020 and references therein). One of the commonly used methods is to find the $Af\rho$ parameter that characterizes the properties of a cometary coma (A'Hearn et al., 1984). This parameter is product of the mean albedo A of cometary dust particles, the filling factor f (the ratio of the total cross section of dust grains in a cometary coma to the area of a projected aperture), and the projected aperture radius ρ (expressed in centimeters) on the picture plane of the comet. It should be stressed that $Af\rho$ describes the properties of a comet itself and is independent of a telescope and an aperture only in the case of steady conditions in the cometary coma (e.g., A'Hearn et al., 1984; Shi et al., 2019). For the *V*-band, it could be determined as.

$$Af\rho = 4R_h^2\Delta^2 \times 10^{0.4(m_{\odot v} - m_{av})} \times \rho^{-1}, \quad (1)$$

where R_h and Δ are the heliocentric and geocentric distances of the comet (expressed in AU and centimeters, respectively); m_{av} and $m_{\odot v}$ are the apparent magnitudes of the comet and the Sun, respectively. Let us calculate this parameter from the photometric data of the considered asteroids.

First, we compute the projected aperture radii ρ for the images of Themis, Hamburga, and Interamnia, which yields 4.8276×10^8, 3.1406×10^8, and 4.3189×10^8 cm, respectively. Then, using the apparent magnitudes of the asteroids on March 17 and the solar apparent magnitude $m_{\odot v} = -26.76^m$ viewed from 1 AU in the photometric system of Vega (Willmer, 2018), we find the $Af\rho$ parameters of the asteroids according to formula (1). The resulting values— 4.2621×10^4 cm (Themis), 3.8348×10^3 cm (Hamburga), and 1.2723×10^5 cm (Interamnia)—are two to three orders of magnitude higher than the values typical of active comets (e.g., A'Hearn et al., 1984). This suggests that the obtained photometric data cannot be used to study the considered asteroids by the cometary methods mentioned above. We see two possible explanations of this result: the seeing conditions during our *UBVRI*-observations of asteroids were not good enough to correctly determine the projected angular aperture radius ρ in the images, as well as the angular resolution of the combination of the telescope and the CCD camera with a specified angular resolution was not high enough to measure the real extent of a subtle exosphere of the asteroid. Also, we failed to identify visual activity of the asteroids through such techniques as the image stacking, because no additional images were available. Unfortunately, the obtained data set was a single one.

However, these *UBVRI*-data (recalculated for the reflectivity at the corresponding effective wavelengths of the filters) were successfully used to determine the main spectral features of the asteroids and to model them, which will be discussed in Section 3. This will also allow us to find a lower estimate of the mass of particles in the asteroid's exosphere (see below, Section 3).

2.4. Main factors of solar activity and their possible influence on simultaneous sublimation activity of main-belt asteroids

It remains to explain the difference in the activity signs of the considered asteroids at perihelion during their observations in 2012 and 2016–2018. From the analysis of their observational conditions, we revealed the influence of solar activity on the spectral signs of sublimation activity of Adeona, Interamnia, and Nina in September 2012:

they turned out to be most prominent at the 11-year solar activity maximum determined from the number of solar spots S_n (http://sidc.oma.be/silso/dayssnplot) (Fig. 3). Besides, as follows from the GOES-15 X-ray satellite records (https://tesis.lebedev.ru/en/sun_flares.html?m=9&d=6&y=2012), our observations in 2012 were performed after a two-week period of frequent solar flares, the intensity of which varied from weak to medium nearly every day (Busarev et al., 2019a). They probably entailed a series of shock waves in the solar wind (SWSWs) produced by coronal mass ejections (CMEs), transforming into interplanetary CMEs (ICMEs) (e.g., Hudson et al., 2006; Webb and Howard, 2012; von Forstner et al., 2018). ICMEs and, consequently, a stronger radiation impact on the asteroid surfaces might have a destructive effect on water ice and other water-containing compounds on primitive asteroids. Additionally, the damage of organic coatings (if present) on the surfaces of ice particles should intensify the ice sublimation. As a result, at that time, we could observe more prominent spectral features that were caused by denser sublimation-driven exospheres of active asteroids. The moment of our observations in 2012 is indicated by a vertical arrow in Fig. 3. As is seen from the same data, solar activity gradually decreased over the 2016–2019 period.

According to numerous satellite measurements, solar flares are often, but not always, accompanied by CMEs, and there is still a lack of understanding how the two phenomena—flares and ejections—are interrelated (e.g., Hundhausen et al., 1994; Subramanian and Dere, 2001; Hudson et al., 2006). Generally, the extremely ionized solar matter, intensively moving in a strong magnetic field in the chromosphere or deeper layers of the solar atmosphere, especially in the vicinity of sunspots, produces a burst of X-ray radiation first and, in 1–2 h, an explosive coronal outburst of magnetized plasma or CME. By common consensus, a key mechanism of this fast motion of plasma and its strong eruption out of the solar atmosphere is the reconnection of magnetic lines of force. It is capable to convert the magnetic energy into the other forms of energy, such as short-wavelength electromagnetic, heat, and kinetic ones (Parker, 1974; Forbes and Priest, 1995; Forbes, 2000; Su et al., 2013; Gou et al., 2019, and references therein).

One more inherent feature of the Sun and, specifically, the solar corona, is its permanent activity in a form of the solar wind (e.g., Parker, 1963; Hundhausen, 1972; Kovalenko, 1983; Marsch, 2006; Pinto et al., 2016). As is well known, there are three constituents in the solar wind. (1) The first one is a constant flux of protons, electrons, alpha-particles and heavier particles. It is called the slow solar wind (with a speed below 550 km/s), because the solar gravitational field cannot hold protons and other particles having a very high temperature (of the order of a few million Kelvins) in the corona, which leads to its continuous expansion

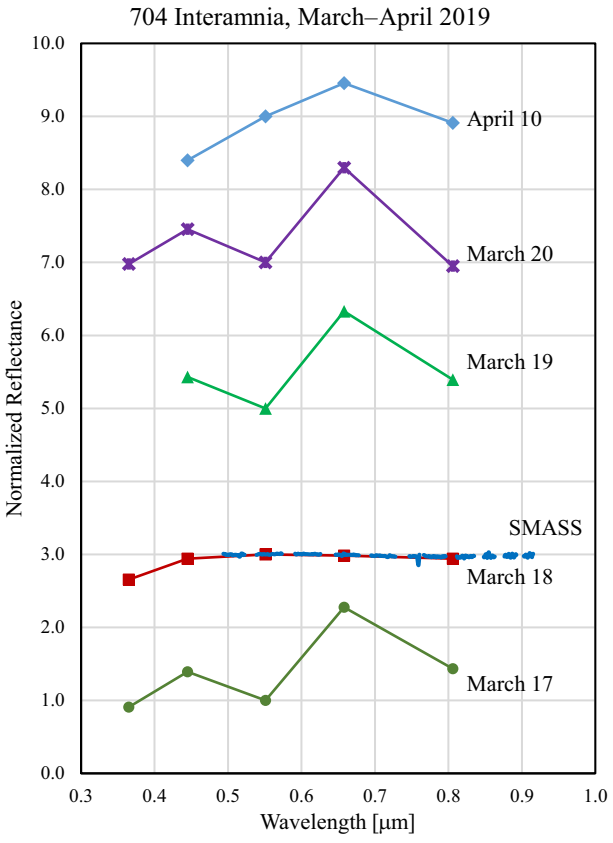

Fig. 6. The reflectance spectra of (704) Interamnia obtained from the *UBVRI* photometric data on March 17–20 and April 10, 2019, when the asteroid was close to perihelion (Busarev et al., 2019b) (Table 2). The spectra are normalized to the value at 0.55 μm and shifted along the vertical axis for clarity. The spectrum measured on March 18, which contains no maxima at 0.45 and 0.66 μm, is compared to the "canonical" one of Interamnia from the SMASS database (https://sbnapps.psi.edu/ferret/; Lazzaro et al., 2006).

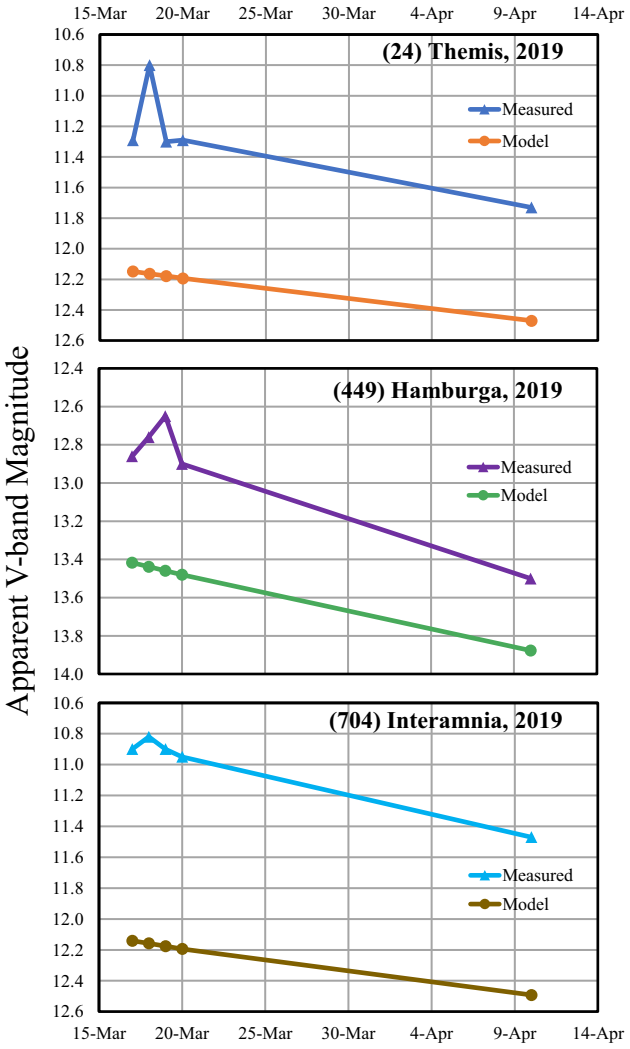

Fig. 7. The apparent *V*-magnitudes of Themis, Hamburga, and Interamnia measured in March–April 2019, which were calculated from observational data with the MaxinDL program (using the nearby standard stars on the same CCD-frames), are systematically lower than ephemeris (model) magnitudes of the asteroids at the same wavelengths according to the IAU MPC and JPL on-line services (Giorgini et al., 1996).

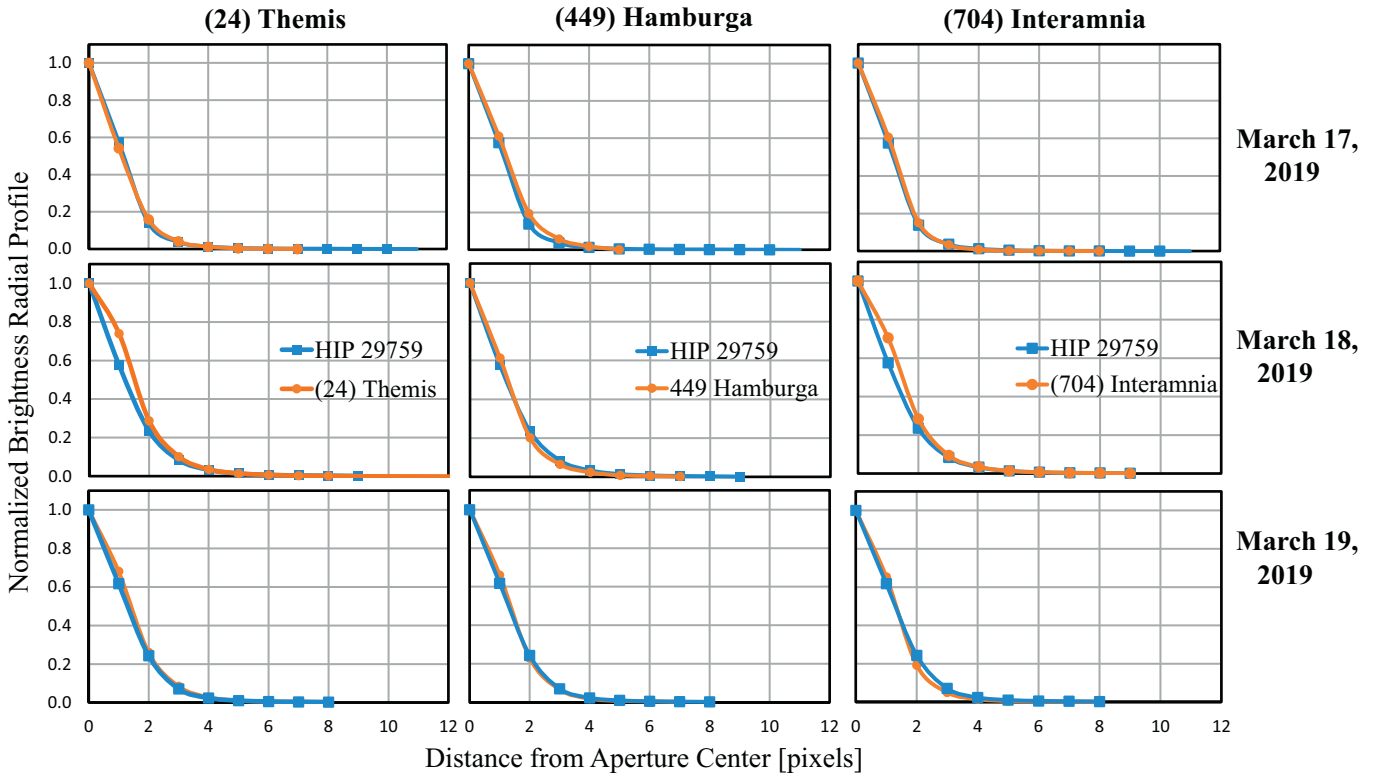

Fig. 8. The radial brightness profiles of Themis, Hamburga, and Interamnia (orange curves) measured on March 17, 18, and 19, 2019 are compared to the profiles of the nearby solar analog star, HIP 29759 (blue curves). The excess of the radial profiles of the asteroids over that of HIP 29759 is largest on March 18 for Themis and Interamnia and on March 19 for Hamburga, which agrees with the lowest apparent magnitudes of the asteroids at the time they experienced the supposed impact of a shock wave of the solar wind (Fig. 7). (For interpretation of the references to colour in this figure legend, the reader is referred to the web version of this article.)

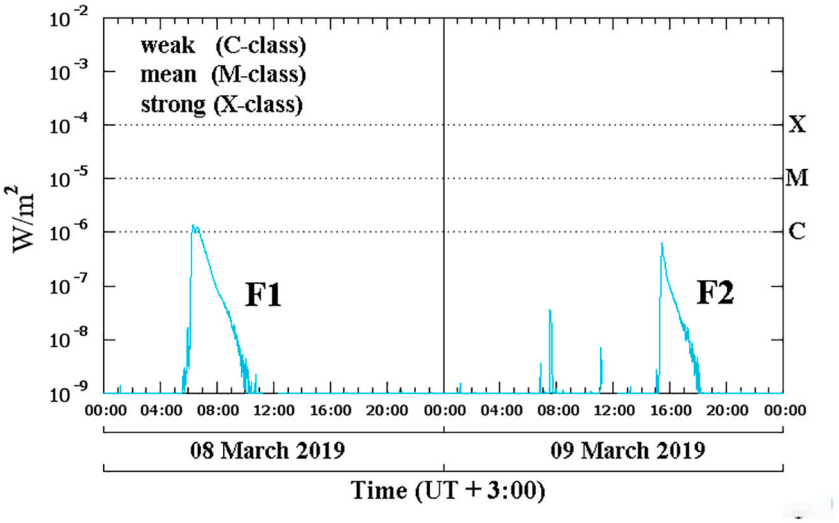

Fig. 9. The intensities of X-ray solar flares (F1 and F2) according to the GOES-15 X-ray satellite archive data (https://tesis.lebedev.ru/en/sun_flares.html?m=3&d=9&y=2019) measured on March 8–9, 2019 and spaced by the 32-h interval. The first one, at UT = 04:17:40 on March 8, was stronger.

into outer space. (2) The second component is quasi-stationary high-speed (with a speed above 550 km/s) solar plasma flows—the so-called fast solar wind. It predominately originates from the coronal holes (well seen in X-ray snapshots of the Sun), where solar magnetic lines of force are non-closed; and these flows are observed at the distances up to several solar radii. (3) The third component includes sporadic high-speed flows and ejections, which are relatively short-term and extremely heterogeneous and complex in structure; they fill the interplanetary space up to the borders of the heliosphere (50–200 AU) (e.g., Parker, 1974; Habbal et al., 1997; Webb and Howard, 2012). CMEs belong to the last category, although their speeds can vary within the widest possible range (of 35 to 1000–1100 km/s) depending on their mass and kinetic energy (e.g., Hundhausen et al., 1994; Borovsky, 2020). ICMEs should also be taken into account as cloud formations; they may be accelerated or de-accelerated not only in the solar corona but in the interplanetary space depending on their structure and the

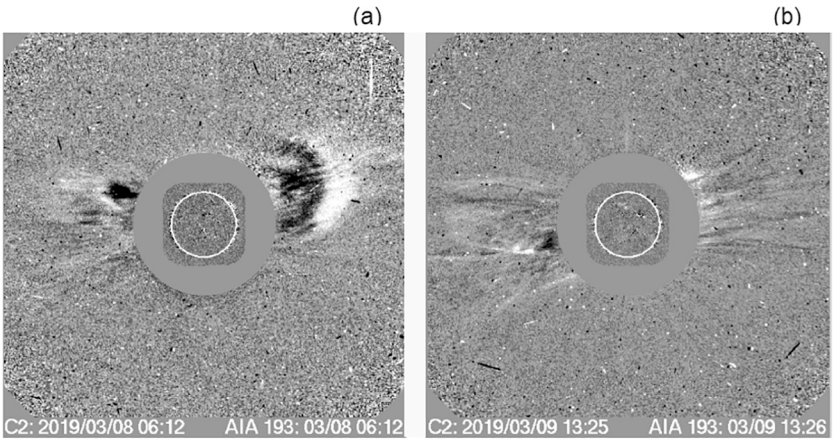

Fig. 10. Coronal mass ejections CME1 (a) and CME2 (b) registered by the Large Angle and Spectrometric Coronagraph (LASCO) onboard the Solar and Heliospheric Observatory (SOHO) (https://cdaw.gsfc.nasa.gov/CME_list/UNIVERSAL/2019_03/univ2019_03.html). They are related to solar flares F1 and F2 (shown in Fig. 7), respectively, which presumably influenced activity of asteroids, (24) Themis, (449) Hamburga, and (704) Interamnia, on March 18, 2019. It can be seen that CME1 and CME2 are close to the equatorial (ecliptic) plane.

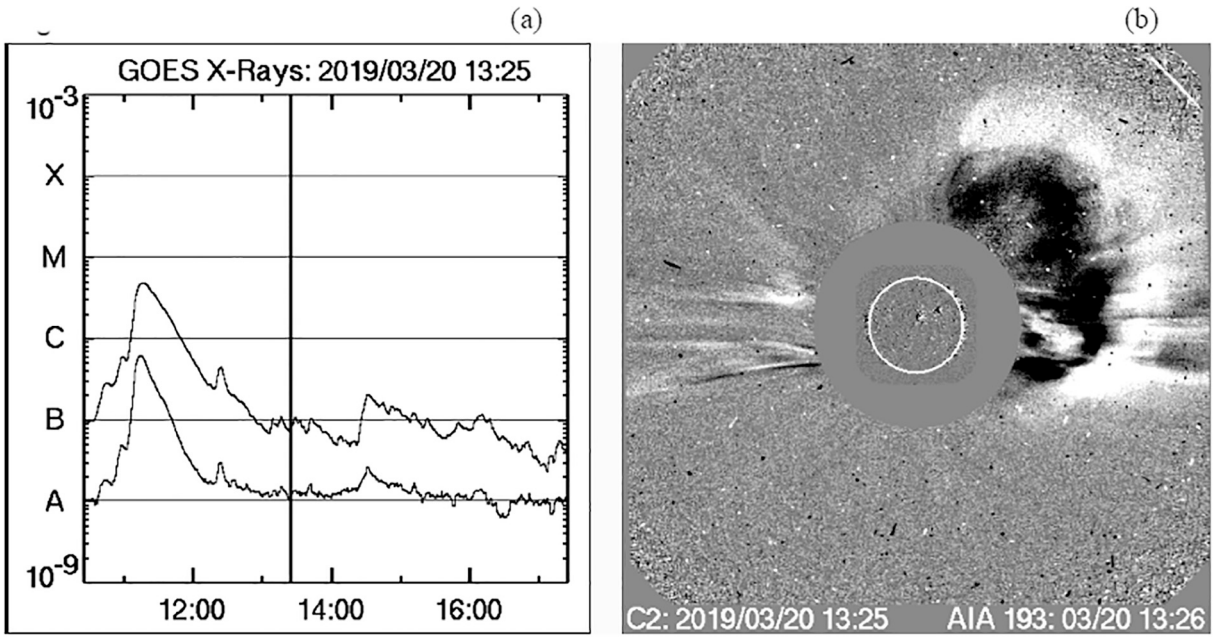

Fig. 11. The intensity of X-ray solar flare (a) coupled with a CME (b), which took place on March 20, 2019 (UT = 11:48:06) in near the ecliptic plane (https://cdaw.gsfc.nasa.gov/CME_list/UNIVERSAL/2019_03/univ2019_03.html) was stronger than those shown in Fig. 8.

structure of surroundings (e.g., Hundhausen and Gosling, 1976; Borovsky, 2020).

Thus, we can summarize some of the above results that are useful for further consideration: (1) the reference speed and density values for the low- and high-speed solar wind measured on the Earth's orbit are v = 327 and 702 km/s and n = 11.9 and 3.9 1/cm^3, respectively (e.g., Kovalenko, 1983); (2) CMEs often accompany solar flares in the form of ejected plasma clumps with the frozen-in magnetic lines of force; (3) ICMEs, the velocity of which is a sum of their own velocity and the angular velocity of the Sun, interact with the spatially inhomogeneous solar-wind streams and produce SWSWs that influence all bodies in the Solar System.

Obviously, it is easier to detect the impact of ICMEs on the exospheres of active asteroids during a period of low solar activity, when they occur is rarely. The influence of SWSWs, which were induced by the solar CMEs closest in time to the measurements, on the spectra of the asteroids is apparently seen in the spectra of March 18, 2019 (Figs. 4–6). Also, according to the apparent magnitudes of the asteroids (Fig. 7), the SWSW impact on the asteroids near the Sun (24 and 449) is stronger than that on more distant one (704) (Table 2), which is in accordance with the weakening of the SWSWs with heliocentric distance. We assumed that the disappearance of the exosphere-induced spectral features on March 18 (Figs. 4–6) was a result of sweeping away the exospheres by a SWSW generated by the CME related to the nearest in time solar flare (Busarev et al., 2019b). To support this supposition, the "canonical" SMASS reflectance spectra of Themis and Interamnia, which were produced only by bare silicate surfaces of the asteroids, are shown together with data of observations of March 18, 2019 in Figs. 4 and 6. We consider the spectra measured on March 18, 2019 and the SMASS spectra to be not influenced by the presence of an exosphere, since they are typical of the reflectance spectra of primitive-type asteroids (C type and close). The latter are similar to the spectra of their nearest analogs – CI and CM meteorites or hydrated minerals (phillosilicates, etc. (e.g., Wagner et al., 1987)) that exhibit a smooth and almost flat (or weakly sloping) continuum in the visible range.

According to the GOES-15 X-ray satellite archive data, there were two

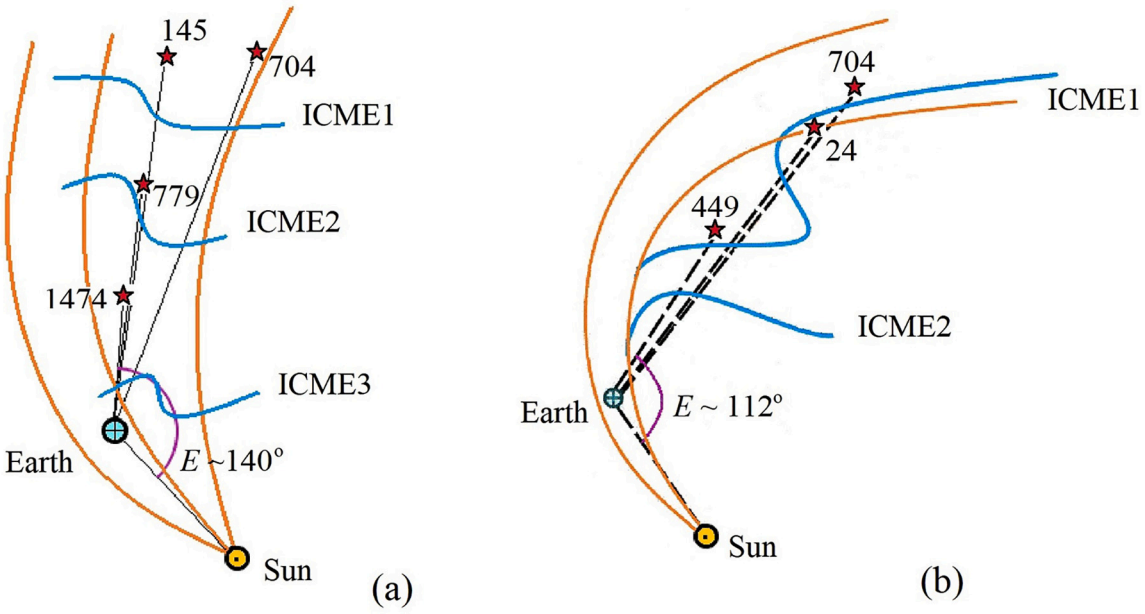

Fig. 12. (a) The positions of (145) Adeona, (704) Interamnia, (779) Nina, and (1474) Baira relative to the Earth and the Sun during our observations in September 2012 are schematically shown together with the supposed profiles of the SWSW fronts (blue lines) produced by several ICMEs and the lines of force of the solar magnetic field (orange lines), which cause nearby ICMEs to move in roughly the same direction during the period of the highest level of solar activity (in 2012–2014). A joined impact of ICME SWSWs on Adeona, Interamnia, Nina, and Baira, being in close directions, made the features in their reflectance spectra more pronounced and similar. (b) The positions of (24) Themis, (449) Hamburga, and (704) Interamnia during our observations in March–April 2019 are also shown together with the supposed profiles of the SWSW fronts, which influence the considered asteroids, and the lines of force of the solar magnetic field, which divide the fast and slow solar wind flows produced by the rotating Sun. (For interpretation of the references to colour in this figure legend, the reader is referred to the web version of this article.)

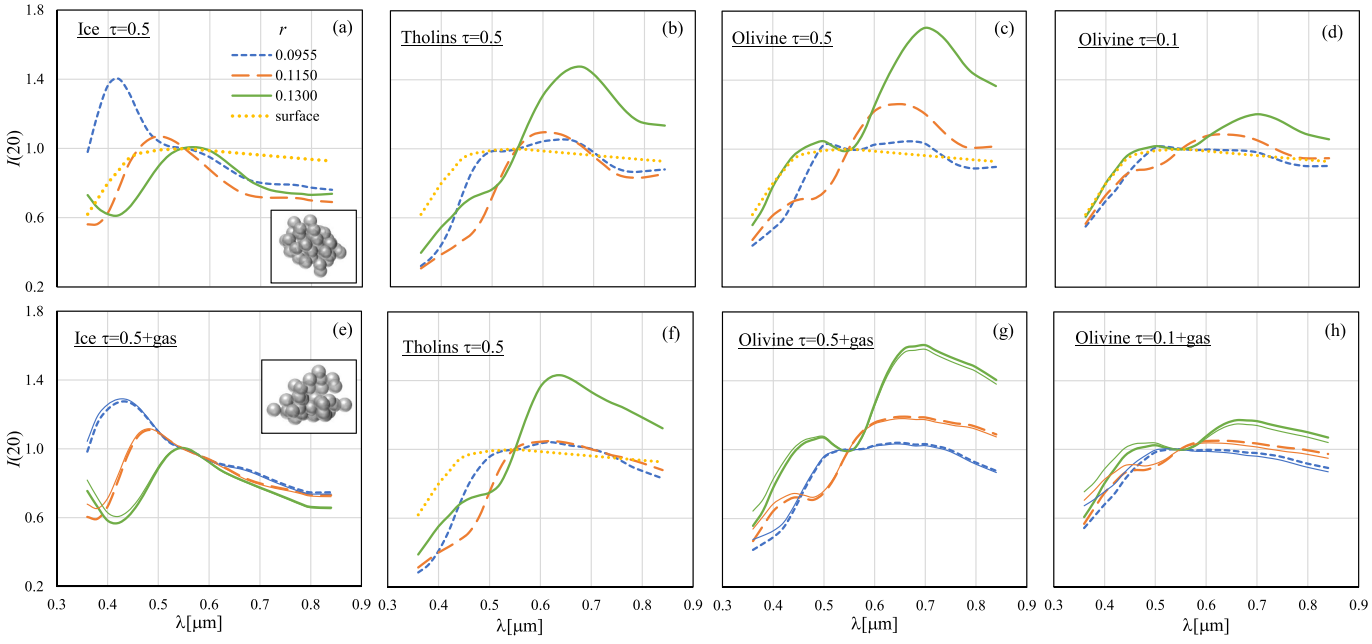

Fig. 13. The spectra of the intensity of light scattered by the exosphere-surface system at a phase angle of 20° $I(20)$ (normalized to the value at $\lambda = 0.55$ μm) and the assumed spectra of the underlying surface. Each of the diagrams contains the spectral curves for three specified radii of aggregate constituent particles (CPs) r in the densely packed ($p = 0.54$, upper row) and more porous ($p = 0.78$, lower row) structures. The number of CPs in clusters are $N = 73$, 42, and 29 for the corresponding CP radii (from 0.0955 to 0.130 μm), which yields $R = 0.4$ μm. Three cases of the material (specified in the diagrams) are shown.

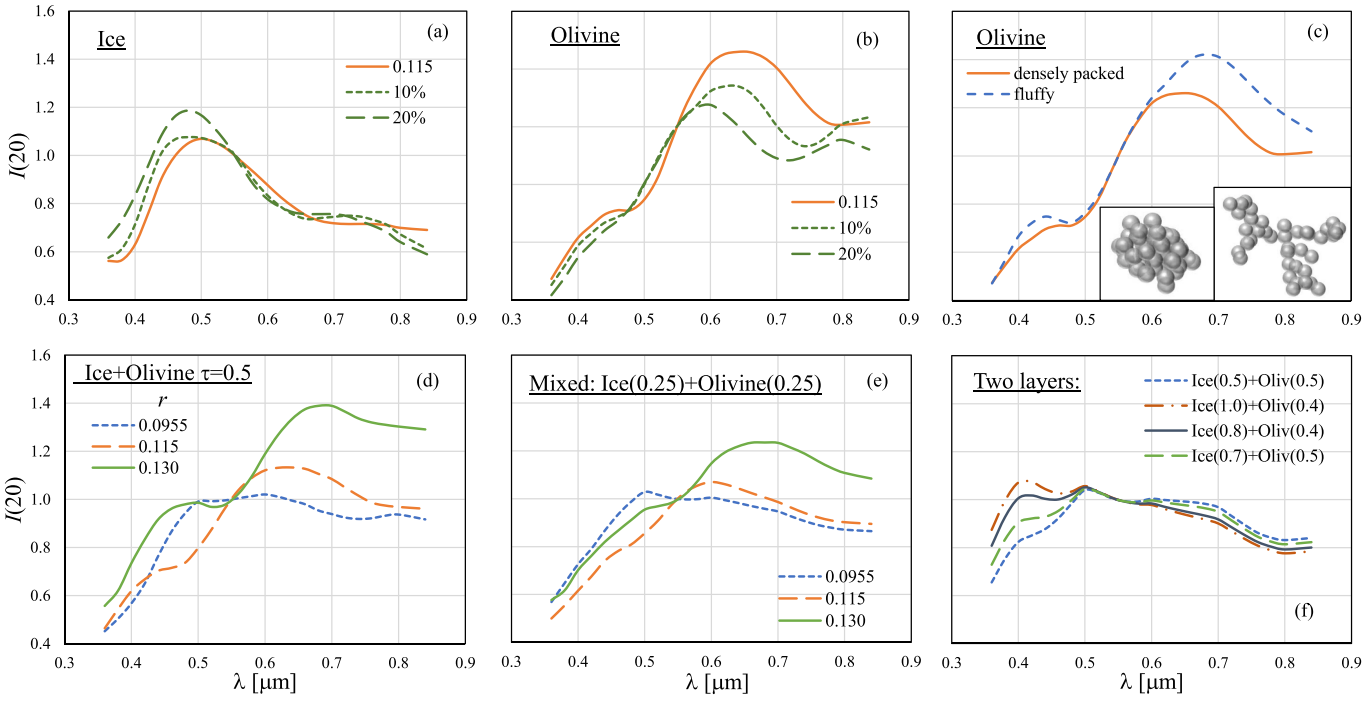

Fig. 14. The normalized reflectance spectra of the exosphere-surface system $I(20)$ for various cases of the properties of clusters in the exosphere with optical thickness $\tau = 0.5$, if not specified differently. (a) The spectra for densely packed clusters ($p = 0.54$) composed of ice monomers ($N = 42$, $r = 0.115$ μm) are compared to those of clusters with the same number of constituents differing in size by ±10 and ± 20% from a mean value of $r = 0.115$ μm. (b) The same as in panel (a) except for olivine constituents. (c) The spectra for densely packed ($p = 0.54$) and fluffy ($p = 0.93$) structures shown in the insets; $N = 42$ and $r = 0.115$ μm. (d) Clusters ($p = 0.54$) contain ice and olivine monomers of specified sizes mixed under proportion 1:1. (e) Clusters ($p = 0.54$) of different composition are homogeneously mixed in the exosphere, the τ values for each of the components are specified in brackets. (f) Clusters ($p = 0.54$) of different composition are separated into layers in the exosphere (the ice layer is below), $r = 0.0955$ μm, and $N = 73$; the τ values for each of the layers are specified in brackets.

weak solar flares spaced by the 32-h interval on March 8–9, 2019; and the first one, at UT = 04:17:40 on March 8, was stronger (https://tesis.lebedev.ru/en/sun_flares.html?m=3&d=9&y=2019) (Fig. 9). Importantly, these solar flares were accompanied by coronal mass ejections (hereafter, CME1 and CME2) registered by the Large Angle and Spectrometric Coronagraph (LASCO) onboard the Solar and Heliospheric Observatory (SOHO); their masses are estimated at 6.4e+14 and 1.9e+14 g, respectively, and they are directed eastward in the near equatorial plane (https://cdaw.gsfc.nasa.gov/CME_list/UNIVERSAL/2019_03/univ2019_03.html) (Fig. 10a and b). This substantiates the origin of SWSWs related to the solar flares that could influence the exospheres of asteroids considered. However, due to a complex structure of the interplanetary magnetic field, it is not clear which of CMEs (CME1 or CME2) swept out the asteroid exospheres on March 18, 2019. According to the mentioned satellite data, there were no other solar flares a month before March 8 and in a period of March 9–18, 2019, corresponding to low solar activity. Nevertheless, a stronger X-ray solar flare coupled with a CME took place on March 20, 2019 (UT = 11:48:06); it was nearly twice as much as CME1 in mass (1.6e+15 g) and width (https://cdaw.gsfc.nasa.gov/CME_list/UNIVERSAL/2019_03/univ2019_03.html) (Fig. 11a and b).

Observations of the considered asteroids on March 19 and March 20 yielded the spectra similar to those of March 17 (see the corresponding profiles in Figs. 4–6), which again demonstrate the presence of tenuous exospheres around asteroids. We will discuss the features of these spectra in more detail in Section 3, which is focused on the modeling of the reflectance spectra of asteroids with an exosphere.

The stronger CME1 SWSW could reach (704) Interamnia, the most distant one of the considered asteroids (the heliocentric distance was 3.16 AU, see Table 2), in ~11 days (from March 8 to March 18), if it propagated with an average speed of ~550 km/s. Since this estimate is consistent with the mean solar wind speed (e.g., Kovalenko, 1983; Hundhausen et al., 1994; Borovsky, 2020), we may conclude that it is a correct choice to assume the CME1 SWSW to be a key factor to influence the exospheres of the observed asteroids. Given the same time for the SWSW to reach (449) Hamburga and (24) Themis (the corresponding heliocentric distances are 2.11 and 2.76 AU, see Table 2) on March 18, we derive the average velocities of the SWSW, propagating toward these asteroids, as ~332 and ~ 434 km/s. At a glance, the disagreement between the SWSW velocities in various directions may seem strange. However, this apparently characterizes the irregular geometrical structure of a CME, which depends on its location on the Sun with respect to coronal holes (sources of the high-speed solar wind) and streamers (sources of the low-speed solar wind). At the same time, the SWSW speed-vs-time profile changes due to the partial deceleration or acceleration of the SWSW front by the interplanetary magnetic field (e.g., Borovsky and Denton, 2016). Particularly, if the SWSWs moved along spiral magnetic lines of force (shown by orange curves in Fig. 12), which divide the fast and slow solar wind flows created by the rotating Sun, they might have different speeds (e.g., Borovsky, 2020).

Fig. 12a and b schematically show the positions of the considered asteroids during our observations in September 2012 (a high level of solar activity) and March–April 2019 (a low level of solar activity), respectively. In Fig. 12, the positions (145) Adeona, (704) Interamnia, (779) Nina, and (1474) Beira (for the latter three ones, the average elongation angle is $E \approx 140°$; see Table 1) (Fig. 12a) and the positions of (24) Themis, (449) Hamburga, and (704) Interamnia (with an average elongation angle of $E \approx 112°$; see Table 2) (Fig. 12b) are shown together with the supposed profiles of the SWSW fronts, which are produced by several ICMEs and move along the lines of force of the solar magnetic field that influences the considered asteroids. It is seen from the figure that a very close coincidence of the directions toward the asteroids (and, consequently, the similarity of elongation values) explains how the

asteroids may successively be subjected to the impact of the SWSWs moving in the same direction along the solar magnetic lines of force. A joint action of the ICMEs, which are close in duration of the period of high solar activity, might trigger sublimation activity of (145) Adeona in 2012, long before its perihelion. The solar activity impact may also explain the similarity in the reflectance spectra (the wavelength positions of the maxima) of active asteroids of close taxonomic types (hence, of similar composition) surrounded by an exosphere developed due to more strong sublimation of ice and the intense solar wind.

To model the SWSW impact produced by a solar CME on an asteroid is beyond the scope of the paper. Here we mostly deal with new spectral data, which contain the indications of activity of asteroids, and model their reflectance spectra on the basis of the light-scattering and radiative-transfer theory. However, we realize that our observational data may be used to assess the approximate energy imparted to an asteroid from the SWSW of the identified CME. The model of an asteroid's exosphere should account for the energy balance to give two values of the total energy of exosphere particles (with and without SWSW influence) providing the estimate of the SWSW action. So, we call for additional modeling work to be done that would incorporate the results from this paper.

3. Numerical simulations and interpretation of the reflectance spectra of active asteroids

3.1. Input parameters for simulations

3.1.1. Particles in the exosphere

To retrieve the properties of exospheres of the active asteroids from their reflectance spectra, we calculated the light-scattering models for particles composing the exosphere. For this, such parameters of particles as their sizes, refractive index, and structure should be specified.

3.1.1.1. Morphology and sizes. First, we assumed that dust/ice particles in the exosphere have a complex (aggregate) structure, as those in comae and tails of comets. An aggregate structure of cometary particles with submicron constituents is confirmed by the results of both remote and in situ investigations of comets in the Solar System (see, e.g., Fulle et al., 2000; Kolokolova et al., 2004; Güttler et al., 2019; and references therein). In particular, according to the polarimetry of comets, the sizes of fragments or heterogeneities in cometary particles are somewhat smaller than or comparable to the visible wavelengths, so that the size parameters of constituents ($x \equiv 2\pi r/\lambda$, where r is the radius of constituents and λ is the wavelength) are in a range of 1.0–2.0 (e.g., Petrova et al., 2000; Kimura et al., 2003; Tishkovets et al., 2004; Lasue et al., 2009; Lumme and Penttilä, 2011; and references therein). For this size relationship between the scatterers and the wavelength, the electromagnetic interaction of constituents in aggregates substantially influences the results of optical measurements, which requires this interaction to be taken into account in the light-scattering model calculations (e.g., Tishkovets et al., 2004; Dlugach et al., 2011; Zubko et al., 2015; Liu and Mishchenko, 2018; Kolokolova et al., 2018).

Based on a statistical fractal structure of cometary dust agglomerates (e.g., Mannel et al., 2016), we use here fractal-like aggregates (clusters) simulated with the diffusion-limited aggregation from identical submicron particles (Mackowski, 1995). Then the resulting structure can be represented by $N = k_f\,(R_g/d)^{Df}$, in which N is the number of spheres composing a cluster (monomers), d is their diameter, R_g is the radius of gyration of the cluster, D_f is the fractal dimension, and k_f is a pre-factor constant.

It is worth stressing that our purpose here is to model the scattering properties of aggregate particles rather than the exosphere particles themselves. Though the latter can be much larger than the structures considered here, the positions of interference features produced by aggregates in the spectra become resistant to the growing of aggregates, if the number of constituent particles (CPs) has reached some value particular to a specified structure (see below). As has been recently shown by Tishkovets and Petrova (2020), in the considered ranges of wavelengths (0.3–0.9 μm) and CP radii (~0.10–0.15 μm), the interference feature positions in the spectra of aggregates mostly depend on the real part of the refractive index and the sizes of CPs rather than their number N. This allows us to consider rather small structures in the analysis of the spectral patterns characteristic of aggregate particles. In the simulations, the CP number varied from 5 to ~250, which provided the radius of the mass-equivalent spheres of clusters up to $R \approx 0.8$ μm. Below, we mostly present the model spectra for clusters with $R = 0.4$ μm.

Since cometary dust agglomerates widely differ in morphology (e.g., Güttler et al., 2019), we selected the fractal parameter values corresponding to rather densely packed and fluffy structures as examples. Most models presented here were calculated for $k_f = 8$ and $D_f = 3.0$ and 2.1. They correspond to the structure porosity $p \approx 0.54$ and 0.78, respectively, if the number of monomers N is around 40–50. The porosity p was defined from the so-called characteristic radius of a cluster $R_c = (5/3)^{1/2} \times R_g$ as $p = 1 - N \times (r/R_c)^3$. Some models were also calculated for very fluffy clusters with $p = 0.93$ ($k_f = 5.8$ and $D_f = 1.9$). The structures are schematically shown as insets in the plots for the corresponding simulated spectra (see Figs. 13a, e, and 14c). As we will see, the choice of a concrete structure is not of key importance for this analysis and the spectra of different structures exhibit close behavior, if the sizes and the real parts of the refractive index of CPs are the same.

To satisfy the limitations imposed by the results of polarimetry on the sizes of constituents of cometary aggregate particles (see above), we choose three values for the monomer radii—r = 0.0955, 0.115, and 0.130 μm—in calculations of the spectra of particles that are presumably present in the exospheres of asteroids. Several models (Fig. 13, 14d, and e) were also calculated for clusters with CPs of different sizes. Though the smallest fragments identified in cometary particles of the 67P coma (e.g., Güttler et al., 2019) are smaller than the CPs considered here (50–200 nm vs. 200–260 nm), the examination of spectra of structures with so small CPs will be of no practical interest for the present study, since the interference spectral features they produce are in the UV range (0.2–0.3 μm) beyond that in the present simulations (0.36–0.85 μm). Consequently, our analysis does not exclude that the CPs in aggregates may contain even smaller heterogeneities.

3.1.1.2. Composition. To model the presence of particles of different composition in the exospheres of asteroids, we consider three cases for the matter of aggregates. (1) H_2O ice as a representative of volatiles; the real part of the refractive index m_r weakly changes from 1.30 to 1.33 in the considered spectral range (Warren and Brandt, 2008), while the imaginary one m_i is negligible (we note that it is still impossible to directly identify the products of sublimation from active asteroids with currently available observational facilities, while it is supposed that various ices, in addition to H_2O, may survive in their subsurface layers (e.g., Snodgrass et al., 2017)). (2) Mg—Fe silicate (olivine) as one of the most abundant components of the cometary dust material; m_r varies from 1.78 to 1.81, while m_i decreases from 0.20 to ~0.07 with increasing λ from 0.35 to 0.7 μm and further changes weakly (Dorschner et al., 1995). (3) A mixture of organic substances, which is collectively known in astronomy as tholins; their refractive index essentially depends on the formation conditions, but they generally exhibit the strongly increasing absorption at short wavelengths, while m_r varies along the spectrum between 1.55 and 1.75 (e.g., West et al., 2014); here we assumed $m_r = 1.65$ and m_i exponentially decreasing from 0.25 to 0.0 with increasing λ in the considered spectral range. The other organics often considered in astronomy, such as, e.g., hydrogenated carbon, are close to olivines and tholins in terms of the refractive indices (e.g., Jenniskens (1993); Greenberg and Li (1996)).

3.1.1.3. Important comments. It is worth noting that, though the

characteristics of the scattered light weakly but depend on realization peculiarities of the aggregate structure with assumed fractal parameters (Tishkovets et al., 2004), we consider here the spectra only for one of the structure realizations. The reason is that our purpose here is to reveal trends in the behavior of the spectra in dependence on the cluster properties rather than to fit quantitatively the measured spectra with the models. Moreover, test calculations performed for several different realizations of the considered structures confirmed that the spectral curves for different of structure realizations exhibit somewhat differing behavior only at wavelengths larger than 0.5 μm (for the considered monomer sizes and materials) and this effect is much weaker than those produced by varying the other parameters of the clusters.

One more item that should be clarified is that we assume the particles composing clusters to be spherical in shape. This assumption is supported by two circumstances. First, it is seen in electronic microscope images of interplanetary and cometary particles that the aggregate constituents are smoothed in shape (e.g., Güttler et al., 2019, and references therein). Second, for aggregates composed of rather small irregular particles with $x < 2$, the scattering characteristics obtained from numerical modeling (e.g., Lumme and Penttilä, 2011; Zubko et al., 2015) and laboratory measurements (Gustafson and Kolokolova, 1999) turned out to be close to those of multi-sphere aggregates. This fact is explained by some blurring out the peculiarities in the scattering on individual spheres of these sizes by near-field effects if the constituents are close to each other in the aggregate.

3.1.2. Exosphere optical thickness

In most models presented below, the optical thickness of the dust/ice exosphere is assumed to be $\tau = 0.1$ or 0.5 at $\lambda = 0.55$ μm; its change along the spectrum is accounted for according to the change in the scattering cross-section of the aggregates. In some models, we assume the exosphere to contain clusters of different types homogeneously mixed or stratified. To analyze the effect of the gaseous component on the exosphere reflectance spectrum, the models for dust/ice particles homogeneously mixed with gas are calculated (Fig. 13e, g, and h). It is assumed that the gas optical thickness is $\tau_{gas} = 0.002$ at 0.55 μm and changes along the spectrum according to the Rayleigh law $\tau_{gas} \sim 1/\lambda^4$.

The specified values of the optical thickness are based on the data for the column density of particles and gas in cometary comae, since these estimates for exospheres of active asteroids are still lacking. For example, the column densities of dust/ice particles obtained for the jets of comet 103P/Hartley 2 (Protopapa et al., 2014) yield the optical thickness of about 0.1, if the sizes of jet particles are assumed to be as those considered in our study. However, in real jets the particles may be much larger than 1–2 μm, which should result in higher values of the optical thickness. From the column density of gases in the coma of comet 67P/Churyumov–Gerasimenko near perihelion (Bockelée-Morvan et al., 2016), it follows that the gas contribution to the coma's optical thickness is negligible. Nevertheless, to show how the scattering by gas may influence the spectra of the exosphere, we specified this quantity nonzero. Since the particles much smaller than the wavelength ($x << 1$) produce a similar spectral effect as the gaseous component, the model accounting for the gas presence also allows us to illustrate the effect of the presence of such particles in the exosphere.

3.1.3. Spectral characteristics of the surface

To calculate the intensity of light scattered in an exosphere above an underlying surface, it is necessary to specify the surface albedo A_s at each of the wavelengths and the surface reflectance law. Here, we assume that $A_s = 0.072$ at $\lambda = 0.55$ μm, which is an intermediate value between the geometric albedos of Themis and Interamnia (0.067 and 0.078, respectively (http://ssd.jpl.nasa.gov/sbdb.cgi#top)). It is worth noting that Interamnia and Themis have the largest diameters among considered asteroids (306.3 and 198 km, respectively, see Tables 1 and 2); and, apparently, their geometry is not extreme (their light curve variations are rather low, less than 0.09 mag (https://minplanobs.org/alcdef/)) https://minplanobs.org/alcdef/php/alcdef_GenerateALCDEFPage.php. The spectral behavior of A_s in the considered range was obtained from the spectra measured for these asteroids on March 18, 2019, which agree with the SMASS data and presumably correspond to the surfaces of asteroids without exospheres (the corresponding lines in Figs. 4 and 6). Since our task is to interpret the results of integral measurements performed relatively far from the opposition (where the opposition effects may induce a substantial enhancement in brightness), we may assume that the asteroid surface scatters light isotropically, which makes the computing procedure much simpler.

3.2. Computational techniques

To calculate the elements of the single-scattering matrix and cross-sections for the generated clusters in random orientation, we use the numerically exact superposition T-matrix method and the corresponding publicly available FORTRAN code (Mackowski and Mishchenko, 1996, 2011). The T-matrix method is one of the most versatile and efficient direct computer solvers of the macroscopic Maxwell equations widely applied to arbitrary multi-sphere configurations.

Then, the resulting single-scattering characteristics of clusters are used in the radiative transfer procedure to compute the intensity of light scattered by the exosphere-surface system. This procedure is based on the invariant imbedding technique described in detail by Mishchenko and Travis (1997 and references therein). Since it deals with plane-parallel scattering layers, we calculate the intensity of scattered radiation for small areas on a sphere approximating the exosphere around the asteroid. The intensity values obtained for these areas (roughly $3^\circ \times 3^\circ$ in latitude and longitude), within which the scattering medium is considered as plane-parallel, were integrated over the sphere with accounting for the phase angle of observations. The models shown below are for a phase angle of 20°. It is worth noting that variations of the phase angle within ±15° weakly influence the shape of the model spectra, since the single-scattering phase functions of the considered aggregates show no strong features in the backscattering domain at each of the considered wavelengths.

3.3. Model results

Examples of the model spectra calculated for different parameters of aggregates in the exosphere above the asteroid surface are shown in Figs. 13 and 14. The optical thickness of the exosphere, the material of aggregates, and the CP radii are specified in the diagrams. The structures of the clusters are schematically shown in the insets.

The behavior of spectra for the considered exosphere-surface system in dependence on the properties of clusters composing the exosphere completely follows the spectral curves of the single-scattering phase functions for the corresponding clusters in the backscattering domain (Tishkovets and Petrova, 2020). The exception is the short-wavelength range, where a rather rapid decrease in the surface albedo diminishes the intensity of light scattered by the exosphere-surface system. According to the recent analysis of the visible spectra of light scattered by aggregates with submicron constituents to the backward hemisphere, these spectra contain the features induced by the interference of waves scattered on both individual CPs and their ensembles, the spectral positions of which are defined by the CP sizes and the real part of the refractive index (Tishkovets and Petrova, 2020). The "individual" extrema are at $\lambda < 0.4$–0.5 μm depending on r and m_r, while the "collective" maximum is at longer wavelengths. For the considered parameters of aggregates, only the collective maxima and the first individual minima fall into the spectral range of observations. It is well seen in the spectral curves in Fig. 13 that the entire interference pattern moves to longer wavelengths with increasing r and m_r, and the cluster porosity is of secondary importance. For example, for ice particles, the collective interference maximum moves from ~0.42 to ~0.55 μm when r increases from 0.0955 to 0.130 μm, and the only individual minimum seen in the

considered range is that for clusters with larger CPs (at ~0.42 μm for r = 0.130 μm). For the higher values of m_r (for tholins and olivines) and r = 0.130 μm, this minimum is already at 0.50–0.55 μm and the maximum is at 0.65–0.70 μm. It is also worth noting that the presence of CO_2 ice, which is a common component of the cometary material, only slightly shifts the interference pattern to longer wavelengths (for the same r values), since its m_r value is ~8% higher than that of H_2O ice.

Some models shown in Fig. 13 illustrate the effect of a gaseous component in the exosphere, which is a somewhat higher intensity level at short wavelengths relative to the models without gas. The larger the portion of gas (or particles much smaller than the wavelength) in the total optical thickness, the stronger the effect. The decrease in the optical thickness of the dust/ice component expectedly makes the spectral features induced by clusters in the exosphere less prominent, while the spectrum of the surface becomes dominant.

The models in Fig. 14a and b demonstrate the influence of polydispersity of aggregate constituents on the spectra resulted: the collective maximum survives, but moves to shorter wavelengths. At the same time, the interference extrema caused by individual constituents become smoother (Tishkovets and Petrova, 2020), though this spectral range is beyond the present analysis.

To illustrate the effect of the aggregate arrangement, which may be observed in the spectra for clusters of strongly differing structures, the model spectra for densely packed and fluffy clusters are compared in Fig. 14c. It is seen that the collective maximum produced by the fluffy cluster is at longer wavelengths than that of the densely packed one composed of the same number of monomers. The explanation is that more constituents are required for fluffy clusters to produce the collective maximum insensitive to the further growth of the ensemble (Tishkovets and Petrova, 2020).

To show how the composition heterogeneity of aggregates in the exosphere influences the reflectance spectra, the models for aggregates composed of ice and olivine monomers (in proportion 1:1) are shown in Fig. 14d. By comparing the models in Fig. 13a and c, we see that the features produced by olivine monomers became less prominent, while the maxima induced by ice monomers became almost smoothed (especially that for r = 0.0955 μm).

The models in Fig. 14e and f were prepared for exospheres containing aggregates of two different compositions—ice and olivine. The features in the spectra for homogeneously mixed ice and olivine aggregates (Fig. 14e) look even smoother than those for clusters with heterogeneous composition (Fig. 14d). However, the features induced by scattering on different components can be made distinguishable if the ice and olivine aggregates are separated into layers in the exosphere. It would be reasonable to assume that the lower layer may contain both ice and olivine particles, while only olivine particles remain in the upper layer, where the ice component has already sublimated. Note that, for example, according to observations of comets 103P and 67P, aggregate particles in the cometary comae evolve with the distance from the nuclei in a similar way (e.g., Protopapa et al., 2014; Lin et al., 2015; Gicquel et al., 2016). To facilitate the comparison, in the models shown in Fig. 14f, the lower layer was assumed to contain only ice particles; and it is seen that a relatively high value of the optical thickness for the ice component allows its characteristic maximum at $\lambda \approx 0.42$ μm to become noticeable in the spectrum of the exosphere-surface system. Importantly, the spectral feature at 0.4–0.5 μm is very similar to that seen in the reflectance spectra of Adeona, Interamnia, and Nina (Fig. 1a–c) and may be a marker of the specified configuration of the asteroid's exosphere. Thus, this case of the model spectra may be of particular interest for the further analysis of the measured reflectance spectra of active asteroids.

3.4. *Explanation of the measured spectra of active asteroids based on the light-scattering simulations*

The unusual features that attract attention in the spectra of active asteroids measured in 2012 (Fig. 1a–c) are bimodal maxima or "steps" approximately at 0.4 and 0.5 μm. According to the results of simulations described above, these features could be caused by the scattering on clusters with ice and silicate constituents of the smallest model sizes (r = 0.0955 μm). The feature at ~0.4 μm is apparently produced by ice particles, while that at ~0.5 μm, by olivine ones. Moreover, these features of the measured spectra may hardly be explained with a homogeneous model of the exosphere and require a two-layer model as those presented in Fig. 14f. For example, the models like those with ice aggregates in the bottom layer (with τ = 0.8 or 0.7) and olivine aggregates above (with τ = 0.4 or 0.5) may provide a good qualitative fit of the reflectance spectra of Adeona, Interamnia, and Nina measured in 2012. As follows also from the simulations, the fall in the reflectance spectra of Adeona, Interamnia, and Nina at $\lambda < 0.4$ μm (Fig. 1a–c) could be caused by either the absorption in silicate or tholin particles on the surface or in the exosphere (e.g., Wagner et al., 1987; Cloutis et al., 2008; West et al., 2014) or the scattering by ice aggregates with small constituents (r = 0.0955 μm), which produces a maximum at ~0.4 μm and a minimum at 0.32 μm (the latter is beyond the range of measurements).

Fig. 1 shows that each of the considered asteroids exhibits its particular features at ~0.35–0.40 μm, which are apparently determined by peculiarities in the composition and morphology of dust/ice clusters in their exospheres. At the same time, Mars-crosser (1474) Beira exhibited similar maxima but shifted to 0.44–0.45 μm and ~ 0.65 μm, respectively. However, the first one is relatively weak and located against the background of the profile generally rising to the short-wavelength end. The simulations show (Figs. 13g, h, and 14) that these features of Beira's spectra can be produced by clusters with larger (r = 0.115–0.130 μm) ice and silicate (olivine) constituents. The latter were transported to the exosphere by intense gas flows (which, in turn, cause a general rise of the profile due to the Rayleigh scattering) induced by a significant increase of the subsolar temperature (Busarev et al., 2016).

Let us analyze in more detail the reflectance spectra of (704) Interamnia (the diameter is D = 306 km), (24) Themis (D = 198 km), and (449) Hamburga (D = 86 km) obtained in March–April of 2019 with the *UBVRI* (or *BVRI*) photometry. Though these reflectance data measured at several wavelengths cannot probably be called "a spectrum" in the full sense, we use this term for convenience. The spectral patterns observed for these asteroids turned out to be very similar (Figs. 4–6). In addition to the physical causes of this similarity, the fact that the measurements were made only at several wavelengths could contribute to smoothing individual features in the spectra. Consequently, we may use these data to describe only a general profile of the reflectance spectra. However, this allows us to consider, as a first approximation, the characteristic spectral maxima at 0.44 and 0.66 μm in the light of the above simulations (see Fig. 13) and to interpret them as a manifestation of an exosphere around each of these asteroids. It should be noted that infrared observations (in the 2–4-μm wavelength range) of (24) Themis, which were performed by two independent research groups (Campins et al., 2010; Rivkin and Emery, 2010), were the first to reveal the presence of water ice and organic compounds on the surface of the asteroid.

The maxima in the spectra of Themis, Hamburga, and Interamnia are somewhat shifted to the longer wavelengths in comparison with similar features in the spectra of active asteroids observed in 2012 (Fig. 1a–c), which may be caused by the presence of clusters with larger constituents (r = 0.115–0.130 μm) in the exospheres. Since these asteroids were observed in 2019 under low solar activity (hence, when the events of solar flares and associated CMEs, ICMEs, and SWSWs were rare), their material, including dust in the exospheres, could be less exposed to radiation than that of asteroids 145, 704 and 779 in 2012. Therefore, we suppose that the sizes, structure, and density of aggregate particles in the exosphere of active asteroids, as the corresponding properties of dust clusters in comets (e.g., Ivlev et al., 2002; Dominik, 2009), are influenced by the radiation conditions and magnetized interplanetary

plasma, which depend on the general level of solar activity and solar eruptive events.

The unusual profile of the reflectance spectra of (704) Interamnia, (24) Themis, and (449) Hamburga measured on April 10, 2019 (the corresponding profiles in Figs. 4–6) with a single maximum (at 0.66 μm) also needs to be explained by taking into account the model results (Fig. 13) and flare and eruption activity of the Sun. These spectral data were obtained 20 days after a noticeable solar flare and the associated CME occurred on March 20, 2019, which was twice as strong as two similar events occurred earlier, on March 8–9 (https://cdaw.gsfc.nasa.gov/CME_list/UNIVERSAL/2019_03/univ2019_03.html). The SWSW caused by this CME was to reach asteroids Themes, Hamburga, and Interamnia on March 31 (with a mean speed estimated at ~550 km/s). That is, 11 days passed between the impact of this SWSW on the asteroids and our observations on April 10. Thus, the two-peak reflectance spectra of the asteroids were obtained 1–2 days after they had been exposed to impact of the passing-by SWSWs (the corresponding profiles in Figs. 4–6). However, the single-peak spectra of April 10, 2019 were obtained 11 days after the last SWSW passage (see the corresponding profiles in Figs. 4–6). Taking into account that, according to the simulations, the maximum at 0.44 μm may result from the light scattering by clusters of ice constituents (with $r = 0.0955$–0.115 μm) (Fig. 13a and e), we suppose that ice clusters may evaporate from the exospheres of asteroids for less than ~10 days. Consequently, the 0.44-μm maximum in the spectra of asteroids disappeared, and only aggregates with a mixture of silicate and organic particles, producing a maximum at 0.66 μm (panels (b)-(c) and (f)-(h) in Fig. 13), could remain in their exospheres.

Thus, according to the results of our modeling (Figs. 13 and 14), the features in the visible reflectance spectra of active main-belt primitive asteroids (145, 704, 779, 1474, 24, and 449) suggest that exospheres, containing aggregates of Fe—Mg silicate, ice, and tholin particles, enveloped these asteroids during the observations. It is worth reminding that the mass of particles escaping from the asteroids cannot be estimated reliably from the present modeling, since the features in the simulated spectra are mostly sensitive to the sizes of monomers composing the aggregates and the real part of their refractive index rather than to the sizes of agglomerates themselves. Nevertheless, we may attempt to find some rough estimates of this parameter.

Though in real exospheres the sizes of agglomerates may be much larger than those considered here, starting from some size (which depends on the refractive index and the ensemble structure), the spectral features become weakly sensitive to the further growth of an agglomerate (Tishkovets and Petrova, 2020). Because of this, in fact, aggregates of small sizes were sufficient for our simulations of the spectra of exospheres. Consequently, we estimated the optical thickness under the assumption that the entire exosphere contains exactly these small aggregates. The point is that the radiative transfer procedure (within which the optical thickness value is specified) requires the single scattering characteristics of particles, for which the spectrum was calculated, i.e., small aggregates. In reality, no doubt, an exosphere should also contain large particles. However, nothing can be said about their sizes from examination of the spectral features.

Nevertheless, if we assume that the exosphere contains only small aggregates, we may roughly estimate the mass of particles in the exosphere from its optical thickness in the following way. In the simplest case, under the assumption that the exosphere contains identical aggregates (e.g., with a radius of the mass-equivalent sphere $R = 0.6$ μm and the mean porosity of $p = 0.7$ (for the considered aggregates the porosity varies from 0.5 to 0.9 (see Section 3.1.1)), the concentration of which does not change with altitude above the surface, the optical thickness may be presented as.

$$\tau = \pi R^2 \times Q_{sca} \times N \times h, \quad (2)$$

where Q_{sca} the scattering efficiency factor of aggregates, N is their number per unit volume, and h is the exosphere height. For the considered clusters of aggregates, Q_{sca} is about 5.0 in the visible range. Then, $N \times h = 0.18 \times 10^{12} \times \tau$ (for sizes expressed in meters). If $\tau = 0.1$, the number of particles in a column of the exosphere above 1 m^2 is $N \times h = 0.18 \times 10^{10}$ m^{-2}. The mass of particles in this column may be estimated from.

$$M = \rho \times (1.0 - p) \times (4/3)\pi R^3 \times 1.8 \times 10^{10}, \quad (3)$$

where ρ is the material density assumed at 1000 kg/m^3, which yields $M = 5 \times 10^{-6}$ kg/m^2. This value may be considered as a reasonable estimate, if we look at the sublimation rate of the MAB active asteroid mentioned by Jewitt (2012): from 10^{-8} to 10^{-4} kg/m^2s.

Obviously, the assumption that only small aggregates are present in the exosphere is not true. The exosphere should undoubtedly contain larger particles. Then, the above estimate can be considered as a lower limit. For example, from the formulas for the optical thickness of an exosphere and the mass of particles composing it, we may derive the ratio for the masses of different particles:

$$M_1/M_2 = (R_1 \times \tau_1)/(R_2 \times \tau_2) \times Q_{sca2}/Q_{sca1} \quad (4)$$

Then, from the comparison of particles with radii of 0.6 and 10 μm, for which $Q_{sca} = 5.0$ and ~ 2.0, respectively (2.0 is the limit, to which Q_{sca} converges with increasing the particle size (e.g., Hansen and Travis, 1974)), we obtain $M_1/M_2 = 0.024(\tau_1/\tau_2)$. In other words, for the same values of τ, the mass of 10-μm particles in an exosphere should be 42 times larger than that of 0.6-μm particles.

4. Discussion

Here we used spectrophotometric methods, which are well known and has been used for a long time in the study of asteroid matter. Therefore, we find it rather strange that nobody so far has applied these methods to searching for signs of activity on asteroids resulting in a temporal tenuous exosphere. Perhaps, this is due to the prevailing opinion about asteroids as atmosphereless bodies. Adhering to this idea, we performed an ordinary spectrophotometric study of the asteroid matter composition and did not formulate a task for detecting the signs of activity on the bodies. However, the unusual spectral features registered on the observed primitive asteroids led us to a supposition that temporal exospheres may exist on these bodies. Our modeling efforts showed that this is likely the case (Section 3). That is why, the list of the objects considered in the paper does not include known active asteroids. Naturally, we plan to include these asteroids in our next observational programs and encourage other observers to use spectral methods to search for the signs of activity on other primitive asteroids.

One more important issue to be explained is the absence of visible signs of activity of considered objects that exhibit spectral signs of activity. As has been discussed above (Section 2.3), the reason of this is an insufficient spatial resolution of modern ground-based telescopes, which do not allow direct (white-light) detection of a rarefied exosphere at asteroids. However, as follows from the modeling of a reflectance spectrum of an asteroid with an exosphere (section 3), such signs could be registered by spectral methods (spectrophotometric or multiband photometric ones).

Our spectrophotometric data also contain a negative example in terms of finding indications of activity on asteroids, which bolsters the use of spectral methods for this purpose. This is the reflectance spectrum of (32) Pomona, S-type asteroid (Tholen, 1989; Bus and Binzel, 2002), which was obtained nearly at the same time as that for (145) Adeona (Busarev et al., 2015, Figs. 2 and 3). These two asteroids were in close orbital configuration (similar heliocentric distances and elongation angles from the Sun), but Adeona's reflectance spectrum exhibited the light scattering maxima of an exosphere, while that of Pomona did not. So, the spectrum of (32) Pomona provides negative/null result in the search for activity by the spectrophotometric method. An additional value of this result is that it points to the effectiveness of spectral

methods in the study of consequences of the SWSW impact on the asteroid matter of different composition: while a highly porous primitive matter (including phyllosilicates and organics) may undergo destruction and sputtering under the action of high-energy particles, turning into the source of an exosphere, a matter formed at high-temperatures likely does not.

The phenomenon of subtle sublimation activity of main-belt primitive asteroids near perihelion with a small rise of subsolar temperature (up to a few dozens of degrees) could be considered as a very early stage of the process. It likely leads to formation of a rarified dust exosphere composed of small dust/ice aggregates. The typical optical thickness of an exosphere around the asteroid may be ~0.1 at $\lambda = 0.55$ μm, and the reflectance spectra exhibit one or two maxima at 0.40–0.50 and/or 0.60–0.70 μm (Busarev et al., 2015). The life-time of the ice component of the dust/ice exosphere should be relatively short because of quick sublimation of H_2O ice at heliocentric distances of the MAB. The next stage of sublimation activity may take place on those main-belt primitive asteroids, the orbits of which are considerably more eccentric. As follows from our observations (Busarev et al., 2018), the growth of the subsolar temperature by approximately a hundred degrees results in the formation of a denser dust exosphere (the optical thickness may reach $\tau \approx 0.5$ at $\lambda = 0.55$ μm) with silicate particles as a predominant component of (e.g., on Beira).

The fact that some main-belt asteroids demonstrate simultaneous sublimation activity near perihelion points to a common origin of the bodies. The asteroids could originate in the vicinity of "snow line" (inside or beyond) providing a considerable percentage of water ice in their material. If the orbital eccentricity of a body is noticeable and the rise of subsolar temperatures induces its sublimation activity, we may detect the presence of ice in its material. At the same time, we are interested in revealing the evolutionary factors that support an increased content of water ice near the surface of primitive asteroids for a long time and/or strengthen or resume their activity. Among such factors for the main-belt asteroids, we chiefly consider mutual collisions and frequent meteoroid impacts, the influence of which lasts throughout a lifetime of these bodies. However, solar activity and, in particular, solar flares accompanied by CMEs and ICMEs and related SWSWs may play a specific role in forming an exosphere of primitive asteroids. Because of the Sun rotation with nearly a month period, the outflow of its plasma generates a spiral interplanetary magnetic field, which forces all charged particles emitted by the Sun to move away from it along spiral trajectories (e.g., Parker, 1963).

The Earth's magnetosphere could be an additional electromagnetic factor that focuses SWSWs and increases the concentration of particles on their fronts. As is known from the results of space research, the Earth's magnetosphere is a cavity formed around the Earth by magnetic lines of force, which are stretched under the pressure of the magnetized solar plasma flux or by sporadic SWSWs (e.g., Hundhausen et al., 1994; Allen and Alfred, 2004; Blanc et al., 2005; Borovsky, 2020). According to the up-to-date measurements and ideas, the Earth's magnetosphere is elongated in the antisolar direction to considerable distances – from ~200 to ~800 radii of the Earth (e.g., Pinto et al., 2016; Witasse et al., 2017; von Forstner et al., 2018). Importantly, it becomes narrower with increasing the geocentric distance, especially under stronger solar activity.

In connection with the discussion about the solar activity impact on active main-belt asteroids, we hypothesize that a rather stable magnetotail of the Earth could direct the flowing solar wind and the emerging SWSWs along almost a straight line and focus them on the main-belt asteroids being in opposition ($E \approx 180°$). This idea was formulated only as a very preliminary one, and it is based on the fact that the Earth's magnetotail is oriented close to the direction toward the asteroids being in opposition at the time of their usual observations (at minimal phase angles). No modeling or calculations have been performed yet. This may be ascertained by spaceborne measurements in the vicinity of the Earth's magnetotail at different heliocentric distances, similar to those of Solar–Terrestrial Relations Observatory (STEREO) (Witasse et al., 2017). However, according to the present analysis, ground-based spectral observations of active main-belt asteroids being near opposition may also contribute to these investigations.

In our view, the most important result of our work is that sublimation activity simultaneously demonstrated by main-belt primitive asteroids near perihelion points to a considerable content of water ice in the material of these bodies. If so, it may be indicative of their common origin. Given the proximity of primitive-type asteroids or their parent bodies to the snow line in the early Solar System (e.g., Safronov, 1969; Lewis, 1974; Makalkin and Dorofeeva, 2009; Bitsch et al., 2015), we may attempt to specify in general the formation mechanism for asteroids of this kind. Basically, there are two formation scenarios for primitive asteroids: (1) their parent bodies could origin in situ within the ring zone bordered outside by the snow line (or within the MAB), and they included a very small portion of water ice; (2) the bodies of stone-ice composition were first formed in Jupiter's formation zone and then ejected from the zone by the growing proto-Jupiter (after its mass had reached several Earth's masses) in all directions, including the MAB (Safronov and Ziglina, 1991). Along with fragmentation and swiping out smaller bodies originally formed in the MAB at collisions, stone-ice bodies might transport to the MAB a large amount of ice and hydrated silicate materials distributed on the surface of all remained objects (Busarev, 2002, 2012, 2016).

Thus, the evolution according to the second scenario could provide a significantly higher amount of ice in the material of surface layers of primitive asteroids than that in the first case. It is better consistent with the phenomenon of simultaneous activity of primitive asteroids considered here. It is worth noting that the second scenario also explains the presence of hydrated silicates and even ices on main-belt asteroids with the high-temperature mineralogy, including M-type ones (Busarev, 1998, 2002, 2016). One more important argument in favor of the second scenario is a general principle of cleaning the formation zones of large planets from small bodies at the stage when the planets have reached a sufficiently large mass. A specific feature of this mechanism is the predominant ejection of small bodies by a host planet (when it had been reached 2–3 the Earth's mass) from its formation zone rather than their accretion (e.g., Safronov, 1969). We can find manifold indications of the latter processes in the present MAB (the absolute majority of main-belt asteroids of irregular shape, a lot of craters covering their surfaces, etc.).

Giving preference to the second of the above scenarios of the origin of primitive asteroids, let us consider the process of temporal sublimation activity and the related appearance and disappearance of an optically thin exosphere on an asteroid. In the case of a significant ice content in the matter of a primitive asteroid (up to ~ several dozens of percent) and noticeable eccentricity of its orbit, sublimation of water ice on or from under its surface should start and strengthen when the asteroid is approaching its perihelion point. When the subsolar temperature grows relatively weakly and the ejection velocity of sublimating sub-micron H_2O particles and carried away silicate dust grains is low, micron-sized agglomerates of these particles should be distributed more or less homogeneously around the asteroid due to its rotation, which will result in an exosphere of a nearly spherical shape. The ice component in the exosphere should rapidly evaporate. According to our results, ice particles would first disappear from an external part of the exosphere for less than ten days. The dust component of the exosphere may exist longer, probably for several months or so. This may explain different spectral features of active asteroids Adeona, Interamnia, and Nina observed during their next perihelion passages in 2016–2018: considerable changes in the reflectance spectra gradients instead of the specific maxima appeared (Busarev et al., 2018, 2019a). We may expect that the ejection of ice-dust particles from the asteroid surface at higher temperatures is close in nature to those in comets, which are beyond the present analysis and specially considered in depth by many authors (e.g., Vincent et al., 2019; Wesołowski et al., 2019; Skorov et al., 2020; and references therein). According to our interpretation, the maxima

positions moved in the spectra of Beira to longer wavelengths (Fig. 1d), which is likely explained by stronger sublimation activity and more intense ejection of silicate dust to the exosphere at the temperature growing by more than a hundred degrees (Busarev et al., 2018), better correspond to the case of cometary activity. At the same time, as follows from our observations, solar activity may change the above scenario. Apparently, SWSWs may induce a renewal of ice sublimation and additional ejection of dust particles to the exosphere of active asteroids, especially in the periods of high solar activity.

5. Conclusions

To explain the phenomenon of active main-belt asteroids, we analyzed the key parameters of the asteroids, activity of which was detected, the main evolutionary factors that influence these bodies, and the recent solar activity factors. Additionally, we carried out numerical simulations of the reflectance spectra for an asteroid surrounded by a dust/ice exosphere with taking into account morphologic, chemical and mineralogical parameters of particles in the exosphere. This allowed us to make the following conclusions:

1. For the first time, a phenomenon of simultaneous sublimation activity was observed in September 2012 on three main-belt primitive asteroids, (145) Adeona, (704) Interamnia, (779) Nina, and Mars-crosser (1474) Beira. In March–April 2019, our observations of (704) Interamnia, (24) Themis, and (449) Hamburga confirmed the existence of this phenomenon (on the latter two objects - for the first time).
2. As follows from our results, the spectral method is the most sensitive one among the other optical methods to search for weak signs of activity on asteroids in the form of an exosphere. The method (including observations and model calculations) allows one to detect a dilute dust exosphere around an active asteroid, the optical thickness of which may be rather small, e.g., $\tau = 0.1$ at $\lambda = 0.55$ μm, and to estimate the composition of submicron dust particles by the refractive index.
3. The comparison of the reflectance spectra of active asteroids and the model ones calculated for fractal-like agglomerates of submicron particles of different composition suggests that exospheres of active asteroids contain particles of H_2O ice, Fe—Mg silicates (e.g., olivine), and/or tholins.
4. The fact that the sublimation-driven exospheres of three main-belt primitive asteroids, (24) Themis, (449) Hamburga, and (704) Interamnia (the last one was from the Sun at 3.17 AU), simultaneously disappeared on March 18, 2019 is likely caused by the SWSW that originated from a weak solar flare associated with the CME of March 8–9, 2019. According to the photometric data (Fig. 7), the impact of the SWSW on the exosphere of Interamnia was weaker, which agrees with the most distant position of the asteroid from the Sun at the moment.
5. Simultaneous sublimation activity demonstrated near perihelion by main-belt primitive asteroids is apparently indicative of the general processes in the Solar System (as well as in exoplanetary systems). The main one among them is likely a common origin of primitive main-belt asteroids beyond the snow line in the early Solar System. Apparently, solar activity (ICMEs and related SWSWs generated by the Sun) regularly influences the sublimation process considered.

Funding

E.V.P. acknowledges the support of Ministry of Science and Higher Education of the Russian Federation under the grant 075-15-2020-780 (N13.1902.21.0039).

Declaration of Competing Interest

None.

Acknowledgements

The authors thank *the reviewers for constructive remarks that helped us to improve the presentation of our results.*

The authors are grateful for the opportunity to perform observations with the 2-m and 0.6-m telescopes at the IA RAS Terskol observatory and the SAI MSU Crimean observatory, respectively.

The authors are also grateful to M. Mishchenko and D. Mackowski for the freely accessible superposition T-matrix and radiative transfer computational codes (https://www.giss.nasa.gov/staff/mmishchenko/t_matrix.html, www.eng.auburn.edu/~dmckwski/scatcodes/, and https://www.giss.nasa.gov/staff/mmishchenko/brf/). E.V.P. appreciates V. Tishkovets (Institute of Radio Astronomy, Kharkiv, Ukraine) for helpful discussions.

References

A'Hearn, M.F., Schleicher, D.G., Feldman, P.D., Millis, R.L., Thompson, D.T., 1984. Comet Bowell 1980B. Astron. J. 89, 579–591.

Alexander, C.M.I'.D., McKeegan, K.D., Altwegg, K., 2018. Water reservoirs in small planetary bodies: Meteorites, asteroids, and comets. Space Sci. Rev. 214 (2018), 36. https://doi.org/10.1007/s11214-018-0474-9.

Allen, V., Alfred, J., 2004. Origins of Magnetospheric Physics. Univ. of Iowa Press, Iowa.

Bitsch, B., Johansen, A., Lambrechts, M., Morbidelli, A., 2015. The structure of proto-planetary discs around evolving young stars. Astron. Astrophys. 575, 28–44.

Blanc, M., Kallenbach, R., Erkaev, N.V., 2005. In solar system magnetospheres (SSR, 116, 227).

Bockelée-Morvan, D., Crovisier, J., Erard, S., Capaccioni, F., Leyrat, C., et al., 2016. Evolution of CO2, CH4, and OCS abundances relative to H2O in the coma of comet 67P around perihelion from Rosetta/VIRTIS-H observations. Mon. Not. R. Astron. Soc. 462 (Suppl_1), S170–S183. https://doi.org/10.1093/mnras/stw2428.

Borovsky, J.E., 2020. What magnetospheric and ionospheric researchers should know about the solar wind. J. Atmosph. Solar-Terr. Phys. 204, 105271.

Borovsky, J.E., Denton, M.H., 2016. The trailing edges of high-speed streams at 1 AU. J. Geophys. Res. Space Physics 121, 6107–6140.

Brunetto, R., Loeffler, M.J., Nesvorný, D., Sasaki, S., Strazzulla, G., 2015. Asteroid surface alteration by space weathering processes. In: Michel, P., et al. (Eds.), Asteroids IV. Univ. of Arizona, Tucson, pp. 597–616.

Bus, S.J., Binzel, R.P., 2002. Phase II of the small main-belt asteroid spectroscopic survey. A feature-based taxonomy. Icarus 158, 146–177.

Bus, S., Binzel, R.P., 2003. 24 Themis average CCD spectrum. EAR-A-I0028-4-SBN0001/SMASSII-V1.0:24_00_TAB. NASA Planetary Data System.

Busarev, V.V., 1998. Spectral features of M-asteroids: 75 Eurydike and 201 Penelope. Icarus 131, 32–40.

Busarev, V.V., 2002. Hydrated silicates on asteroids of M-, S-, and E- types as possible traces of collisions with bodies of the Jupiter growth zone. Solar Sys. Res. 36, 39–47.

Busarev, V.V., 2012. A hypothesis on the origin of C-type asteroids and carbonaceous chondrites. Conf. "asteroids, comets, meteors 2012" abs. #6017. https://arxiv.org/ftp/arxiv/papers/1211/1211.3042.pdf.

Busarev, V.V., 2016. New reflectance spectra of 40 asteroids: a comparison with previous results and interpretation. Solar Sys. Res. 50, 13–23.

Busarev, V.V., Barabanov, S.I., Rusakov, V.S., Puzin, V.B., Kravtsov, V.V., 2015. Spectrophotometry of (32) Pomona, (145) Adeona, (704) Interamnia, (779) Nina, (330825) 2008 XE3, and 2012 QG42 and laboratory study of possible analog samples. Icarus 262, 44–57.

Busarev, V.V., Barabanov, S.I., Puzin, V.B., 2016. Material composition assessment and discovering sublimation activity on asteroids 145 Adeona, 704 Interamnia, 779 Nina, and 1474 Beira. Sol. Syst. Res. 50, 281–293.

Busarev, V.V., Makalkin, A.B., Vilas, F., Barabanov, S.I., Scherbina, M.P., 2018. New candidates for active asteroids: Main-belt (145) Adeona, (704) Interamnia, (779) Nina, (1474) Beira, and near-earth (162,173) Ryugu. Icarus 304, 83–94.

Busarev, V.V., Shcherbina, M.P., Barabanov, S.I., et al., 2019a. Confirmation of the sublimation activity of the primitive Main-Belt asteroids 779 Nina, 704 Interamnia, and 145 Adeona, as well as its probable spectral signs on 51 Nemausa and 65 Cybele. Sol. Syst. Res. 53, 261–277.

Busarev, V.V., Scherbina, M.P., Irsmambetova, T.R., 2019b. 10th Moscow Solar System Symp. (10MS3), Moscow, Abstr. #10MS3-SW-07.

Campins, H., et al., 2010. Water ice and organics on the surface of the asteroid 24 Themis. Nature 464, 1320–1321. https://doi.org/10.1038/nature09029.

Chandler, C.O., Curtis, A.M., Mommert, M., Sheppard, S.S., Trujillo, C.A., 2018. SAFARI: searching asteroids for activity revealing indicators. PASP 130, 114502 (16 pp).

Chandler, C.O., Kueny, J.K., Trujillo, C.A., Trilling, D.E., Oldroyd, W.J., 2020. Cometary activity discovered on a distant centaur: a nonaqueous sublimation mechanism. Aph J. L. 892, L38 (13 pp).

Cloutis, E.A., McCormack, K.A., Bell III, J.F., et al., 2008. Ultraviolet spectral reflectance properties of common planetary minerals. Icarus 197, 321–347.

Dermott, S.F., Nicholson, P.D., Burns, J.A., Houck, J.R., 1984. Origin of the solar system dust bands discovered by IRAS. Nature 312, 505–509.
Dlugach, J.M., Mishchenko, M.I., Mackowski, D.W., 2011. Numerical simulations of single and multiple scattering by fractal ice clusters. Quant. Spectrosc. Rad. Trans. 112 (11), 1864–1870. https://doi.org/10.1016/j.jqsrt.2011.01.038.
Dodd, R.T., 1981. Meteorites - A Petrologic-Chemical Synthesis. Cambridge Univ, Press, Cambridge.
Dodson-Robison, S.E., et al., 2009. Ice lines, planetesimal composition and solid surface density in the solar nebula. Icarus 200, 672–693.
Dominik, C., 2009. Physical processes: dust coagulation and fragmentation. In: Henning, Th., Grün, E., Steinacker, J. (Eds.), Cosmic Dust—Near and Far, 414. ASP Conference Series, pp. 494–508.
Dorschner, J., Begemann, B., Henning, T., Jaeger, C., Mutschke, H., 1995. Steps toward interstellar silicate mineralogy. II. Study of Mg-Fe-silicate glasses of variable composition. Astron. Astrophys. 300, 503–520.
Durda, D.D., Dermott, S.F., 1997. The collisional evolution of the asteroid belt and its contribution to the zodiacal cloud. Icarus 130, 140–164.
Forbes, T.G., 2000. A review on the genesis of coronal mass ejections. J. Geophys. Res. 105, 23,153–23,165.
Forbes, T.G., Priest, E.R., 1995. Photospheric magnetic field evolution and eruptive flares. Astrophys. J. 6, 377–389.
Fulle, M., Levasseur-Regourd, A.C., McBride, N., Hadamcik, E., 2000. In-situ dust measurements from within the coma of 1P/Halley: first-order approximation with a dust dynamical model. Astron. J. 119, 1968–1977. https://doi.org/10.1086/301285.
Gaffey, M.J., Bell, J.F., Cruikshank, D.P., 1989. Reflectance spectroscopy and asteroid surface mineralogy. In: Binzel, R.P., Gehrels, T., Mattews, M.S. (Eds.), Asteroids II. Univ. of Arizona Press, pp. 98–127.
Gaffey, M.J., Cloutis, E.A., Kelley, M.S., Reed, K.L., 2002. Mineralogy of asteroids. In: Bottke, W.F., Cellino, A., Paolicchi, P., Binzel, R.P. (Eds.), Asteroids III. Univ. of Arizona Press, pp. 183–204.
Gicquel, A., Vincent, J.-B., Agarwal, J., et al., 2016. Sublimation of icy aggregates in the coma of comet 67P/Churyumov-Gerasimenko detected with the OSIRIS cameras onboard Rosetta. Mon. Not. R. Astron. Soc. 462 (Suppl_1), S57–S66. https://doi.org/10.1093/mnras/stw2117.
Giorgini, J.D., Yeomans, D.K., Chamberlin, A.B., et al., 1996. JPL's on-line solar system data service. Bull. Am. Astron. Soc. 28, 1158.
Gou, T., Liu, R., Kliem, B., Wang, Y., Veronig, A.M., 2019. The birth of a coronal mass ejection. Sci. Adv. 5, eaau7004 (9 p.).
Greenberg, J.M., Li, A., 1996. What are the true astronomical silicates? Astron. Astrophys. 309, 258–266.
Gustafson, B.A.S., Kolokolova, L., 1999. A systematic study of light scattering by aggregate particles using the microwave analog technique: angular and wavelength dependence of intensity and polarization. J. Geophys. Res. 104 (D24), 31711–31720. https://doi.org/10.1029/1999JD900327.
Güttler, C., Mannel, T., Rotundi, A., Merouane, S., Fulle, M., et al., 2019. Synthesis of the morphological description of cometary dust at comet 67P/Churyumov-Gerasimenko. Astron. Astrophys. 630, A24. https://doi.org/10.1051/0004-6361/201834751.
Habbal, S.R., et al., 1997. Origins of the slow and the ubiquitous fast solar wind. Astrophys. J. 489, L103–L106.
Hansen, J.E., Travis, L.D., 1974. Light scattering in planetary atmospheres. Space Sci. Rev. 16, 527–610.
Hardorp, J., 1980. The sun among the stars. III. Energy distributions of 16 northern G-type stars and the solar flux calibration. Astron. Astrophys. 91, 221–232.
Hsieh, H.H., Haghighipour, N., 2016. Potential Jupiter-family comet contamination of the main asteroid belt. Icarus 277, 19–38.
Hsieh, H.H., Jewitt, D., 2006. A population of comets in the main asteroid belt. Science 312, 561–563.
Hudson, H.S., Bougeret, J.-L., Burkepile, J., 2006. Coronal mass ejections: overview of observations. Space Sci. Rev. 123, 13–30.
Hundhausen, A.J., 1972. Corona expansion and solar wind. In: Physics and Chemistry in Space, v. 5. Springer-Verlag, Berlin. ISBN-13:978-3-642-65416-9.
Hundhausen, A.J., Gosling, J.T., 1976. Solar wind structure at large heliocentric distances: an interpretation of Pioneer 10 observations. J. Gephys. Res. Space Phys. 81, 1436–1440.
Hundhausen, J., Burkepile, J.T., Cyr, O.C.St, 1994. Speeds of coronal mass ejections: SMM observations from 1980 and 1984–1989. J. Geophys. Res.-Atmos. 99, 6543–6552.
Ivlev, A.V., Morfill, G.E., Konopka, U., 2002. Coagulation of charged microparticles in neutral gas and charge-induced gel transitions. Phys. Rev. Lett. 89 (19), 195502. https://doi.org/10.1103/PhysRevLett.89.195502.
Jarosewich, E., 1990. Chemical analyses of meteorites: a compilation of stony and iron meteorite analyses. Meteoritics 25, 323–337.
Jenniskens, P., 1993. Optical constants of organic refractory residue. Astron. Astrophys. 274, 653–661.
Jewitt, D., 2009. The active centaurs. Astron. J. 137, 4296–4312.
Jewitt, D., 2012. The active asteroids. Astron. J. 143, 66 (14 pp). https://doi.org/10.1088/0004-6256/143/3/66.
Jewitt, D., Li, J., 2010. Activity in Geminid parent (3200) Phaethon. Astron. J. 140, 1519–1527.
Jewitt, D., Agarwal, J., Peixinho, N., et al., 2015. New active asteroid 313P/Gibbs. Astron. J. 149, 81 (9 pp).
Kimura, H., Kolokolova, L., Mann, I., 2003. Optical properties of cometary dust: constrains from numerical studies on light scattering by aggregate particles. Astron. Astrophys. 407, L5–L8. https://doi.org/10.1051/0004-6361:20030967.
Kolokolova, L., Kimura, H., Mann, I., 2004. Characterization of dust particles using photopolarimetric data: Example of cometary dust. In: Mishchenko, M. (Ed.), Videen, G., Yatskiv, Ya. Kluwer Academic Publishers, Dordrecht, The Netherlands, Photopolarimetry in Remote Sensing, pp. 431–454. https://doi.org/10.1007/1-4020-2368-5_20.
Kolokolova, L., Nagdimunov, L., Mackowski, D., 2018. Light scattering by hierarchical aggregates. J. Quant. Spectrosc. Radiat. Transf. 204, 138–143. https://doi.org/10.1016/j.jqsrt.2017.09.019.
Kovalenko, V.A., 1983. Solar Wind. Nauka, Moscow (in Russian).
Küppers, M., O'Rourke, L., Bockelée-Morvan, D., et al., 2014. Localized sources of water vapour on the dwarf planet (1) Ceres. Nature 505, 525–527.
Lasue, J., Levasseur-Regourd, A.C., Hadamcik, E., Alcouffe, G., 2009. Cometary dust properties retrieved from polarization observations: application to C/1995 O1 Hale–Bopp and 1P/Halley. Icarus 199, 129–144. https://doi.org/10.1016/j.icarus.2008.09.008.
Lazzaro, D., Angeli, C.A., Carvano, J.M., Mothe-Diniz, T., Duffard, R., Florczak, M., 2006. Small Solar System Objects Spectroscopic Survey V1.0. EAR-A-I0052-8-S3OS2-V1.0. NASA Planetary Data System.
Lewis, J.S., 1974. The temperature gradient in the solar nebula. Science 186, 440–442.
Lin, Z.-Y., Ip, W.-H., Lai, I.-L., Lee, J.-C., Vincent, J.-B., et al., 2015. Morphology and dynamics of the jets of comet 67P/Churyumov-Gerasimenko: early-phase development. Astron. Astrophys. 583, A11. https://doi.org/10.1051/0004-6361/201525961.
Liu, L., Mishchenko, M.I., 2018. Scattering and radiative properties of morphologically complex carbonaceous aerosols: a systematic modeling study. Remote Sens. 10, 1634. https://doi.org/10.3390/rs10101634.
Lumme, K., Penttilä, A., 2011. Model of light scattering by dust particles in the solar system: applications to cometary comae and planetary regoliths. J. Quant. Spectrosc. Radiat. Transf. 112, 1658–1670. https://doi.org/10.1016/j.jqsrt.2011.01.016.
Mackowski, D.W., 1995. Electrostatics analysis of sphere clusters in the Rayleigh limit: application to soot particles. Appl. Opt. 34, 3535–3545. https://doi.org/10.1364/AO.34.003535.
Mackowski, D.W., Mishchenko, M.I., 1996. Calculation of the T matrix and the scattering matrix for ensembles of spheres. J. Opt. Soc. Am. A. 13, 2266–2278. https://doi.org/10.1364/JOSAA.13.002266.
Mackowski, D.W., Mishchenko, M.I., 2011. A multiple sphere T-matrix Fortran code for use on parallel computer clusters. J. Quant. Spectrosc. Radiat. Transf. 112, 2182–2192. https://doi.org/10.1016/j.jqsrt.
Makalkin, A.B., Dorofeeva, V.A., 2009. Temperature distribution in the solar nebula at successive stages of its evolution. Solar Sys. Res. 43, 508–532.
Mannel, T., Bentley, M.S., Schmied, R., Jeszenszky, H., Levasseur-Regourd, A.C., Romstedt, J., Torkar, K., 2016. Fractal cometary dust – a window into the early solar system. Mon. Not. R. Astron. Soc. 462, S304–S311. https://doi.org/10.1093/mnras/stw2898.
Marsch, E., 2006. Kinetic physics of the solar corona and solar wind. Living Rev. Solar Phys. 3, 1–100.
Masiero, J.R., Grav, T., Mainzer, A.K., Nugent, C.R., Bauer, J.M., Stevenson, R., Sonnett, S., 2014. Astrophys. J. 791, 121–131.
Meech, K.J., Belton, M.J.S., 1990. The atmosphere of 2060 Chiron. Astron. J. 100, 1323–1393.
Meech, K.J., Jewitt, D., Ricker, G.R., 1986. Early photometry of comet P/Halley: development of the coma. Icarus 66, 561–574.
Mishchenko, M.I., Travis, L.D., 1997. Satellite retrieval of aerosol properties over ocean using polarization as well as intensity of reflected sunlight. J. Geophys. Res. 102 (D14), 16989–17013. https://doi.org/10.1029/96JD02425.
Musiichuk, E.Yu., Borysenko, S.A., 2019. Some peculiarities of activity for comets with orbits on 2–5AU. Adv. Astron. S. Ph. 9, 3–7.
Nesvorný, D., Brož, M., Carruba, V., 2015. Identification and dynamical properties of asteroid families. In: Michel, P., DeMeo, F.E., Bottke, W.F. (Eds.), Asteroids IV. Univ. of Arizona Press, Tucson, pp. 297–321.
Nilsson, H., Wieser, G.S., Behar, E., et al., 2015. Evolution of the ion environment of comet 67P/Churyumov-Gerasimenko. Observations between 3.6 and 2.0 AU. Astron. Astrophys. 583 (A20) (8 pp.).
Parker, E.N., 1963. The solar-flare phenomenon and the theory of reconnection and annihilation of magnetic fields. Astrophys. J. Suppl. 8, 177–211.
Parker, E.N., 1974. The dynamical properties of twisted ropes of magnetic field and the vigor of new active regions on the sun. Astrophys. J. 191, 245–254.
Petrova, E.V., Jockers, K., Kiselev, N.N., 2000. Light scattering by aggregates with sizes comparable to the wavelength: an application to cometary dust. Icarus 148, 526–536. https://doi.org/10.1006/icar.2000.6504.
Philippe, S., Schmitt, B., Beck, P., Brissaud, O., 2015. Sublimation of CO_2 ice with H_2O ice contamination: analogy with the sublimation of Mars seasonal caps. 46th Lunar and Planetary Science Conference, held March 16-20, 2015 in The Woodlands, Texas. LPI Contribution No. 1832, Abstract #2559. Abstract #2559.
Pinto, R.F., Brun, A.S., Rouillard, A.P., 2016. Flux-tube geometry and solar wind speed during an activity cycle. Astron. Astrophys. 592, A65.
Poch, O., Pommerol, A., Jost, B., Carrasco, N., Szopa, C., Thomas, N., 2016. Sublimation of ice-tholins mixtures: a morphological and spectro-photometric study. Icarus 266, 288–305.
Protopapa, S., Sunshine, J.M., Feaga, L.M., Kelley, M.S.P., A'Hearn, M.F., et al., 2014. Water ice and dust in the innermost coma of comet 103P/Hartley 2. Icarus 238, 191–204. DOI:10.1016/j.icarus.2014.04.008, 1406.3382.
Rivkin, A.S., Emery, J.P., 2010. Detection of ice and organics on an asteroidal surface. Nature 464, 1322–1323. https://doi.org/10.1038/nature09028.

Safronov, V.S., 1969. Evolution of the Protoplanetary Cloud and the Formation of the Earth and Planets Moscow: Nauka, p. 244 (in Russian) [NASA TTF-667 (Engl. transl.), 1972].
Safronov, V.S., Ziglina, I.N., 1991. Origin of the asteroid belt. Sol. Syst. Res. 25, 139–146.
Schorghofer, N., 2016. Predictions of depth-to-ice on asteroids based on an asynchronous model of temperature, impact stirring, and ice loss. Icarus 276, 88–95.
Shepard, M.K., et al., 2010. A radar survey of M- and X-class asteroids II. Summary and synthesis. Icarus 208, 221–237.
Shi, J.C., Ma, Y.H., 2015. CCD photometry of active centaur 166P/2001 T4 (NEAT). Mon. Not. R. Astron. Soc. 454, 3635–3640.
Shi, J., Ma, Y., Liang, H., Xu, R., 2019. Research of activity of Main Belt Comets 176P/LINEAR, 238P/Read and 288P/(300163) 2006 VW139. Sci. Report. 9, 5492. https://doi.org/10.1038/s41598-019-41880-0.
Skorov, Yu., Keller, H.U., Mottola, S., Hartogh, P., 2020. Near-perihelion activity of comet 67P/Churyumov–Gerasimenko. A first attempt of non-static analysis. Mon. Not. R. Astron. Soc. 494, 3310–3316. https://doi.org/10.1093/mnras/staa865.
Snodgrass, C., et al., 2017. The Main Belt Comets and ice in the Solar System. Astron. Astrophys. Rev. 25 https://doi.org/10.1007/s00159-017-0104-7, 5(59 pp).
Su, Y., et al., 2013. Imaging coronal magnetic-field reconnection in a solar flare. Nat. Phys. Lett. 9, 489–493.
Subramanian, P., Dere, K.P., 2001. Source regions of coronal mass ejections. Astrophys. J. 561, 372–395.
Tholen, D.J., 1989. Asteroid taxonomic classifications. In: Binzel, R.P., Gehrels, T., Mattews, M.S. (Eds.), Asteroids II. Univ. of Arizona Press, pp. 1139–1150.
Tishkovets, V.P., Petrova, E.V., 2020. Spectra of light reflected by aggregate structures of submicron particles. J. Quant. Spectrosc. Radiat. Transf. 252, 107116. https://doi.org/10.1016/j.jqsrt.2020.107116.
Tishkovets, V.P., Petrova, E.V., Jockers, K., 2004. Optical properties of aggregate particles comparable in size to the wavelength. J. Quant. Spectrosc. Radiat. Transf. 86, 241–265. https://doi.org/10.1016/j.jqsrt.2003.08.003.
Vincent, J., Farnham, T., Kührt, E., Skorov, Yu., Marschall, R., Oklay, N., El-Maarry, M. R., Keller, H.U., 2019. Local manifestations of cometary activity. Space Sci. Rev. 215, 30. https://doi.org/10.1007/s11214-019-0596-8.
von Forstner, J.L.F., et al., 2018. Using forbush decreases to derive the transit time of ICMEs propagating from 1 AU to mars. J. Geophys. Res. Space Physics 123, 39–56.
Wagner, J.K., Hapke, B.W., Wells, E.N., 1987. Atlas of reflectance spectra of terrestrial, lunar, and meteoritic powders and frosts from 92 to 1800 NM. Icarus 69, 14–28.
Warner, B.D., Harris, A.W., Pravec, P., 2009. The asteroid lightcurve database. Icarus 202, 134–146.
Warren, S.G., Brandt, R.E., 2008. Optical constants of ice from the ultraviolet to the microwave: a revised compilation. J. Geophys. Res. 113, D14220 https://doi.org/10.1029/2007JD009744.
Webb, D.F., Howard, T.A., 2012. Coronal mass ejections: observations. Living Rev. Solar Phys. 9, 3–83.
Wesołowski, M., Gronkowski, P., Tralle, I., 2019. Selected mechanisms of matter ejection out of the cometary nuclei. Icarus 338, 113546. https://doi.org/10.1016/j.icarus.2019.113546.
West, R., Lavvas, P., Anderson, C., Imanaka, H., 2014. Titan's haze. In: Müller-Wodarg, I., Griffith, C.A., Lellouch, E., Cravens, T.E. (Eds.), Titan: Interior, Surface, Atmosphere, and Space Environment. Cambridge University Press, Cambridge, UK, pp. 285–321. https://doi.org/10.1017/CBO9780511667398.011.
Willmer, C.N.A., 2018. The absolute magnitude of the sun in several filters. Astrophys. J. Suppl. 236, 47 (14 pp).
Witasse, O., Sánchez-Cano, B., Mays, M.L., et al., 2017. Interplanetary coronal mass ejection observed at STEREO-A, Mars, comet67P/Churyumov-Gerasimenko, Saturn, and New Horizons en route to Pluto: comparison of its Forbush decreases at 1.4, 3.1, and 9.9 AU. J. Geophys. Res. Space Physics 122, 7865–7890.
Zacharias, N., Monet, D.G., Levine, S.E., et al., 2004. The naval observatory merged astrometric dataset (NOMAD). Bull. Am. Astron. Soc. 36, 1418.
Zubko, E., Shkuratov, Yu., Videen, G., 2015. Effect of morphology on light scattering by agglomerates. J. Quant. Spectrosc. Radiat. Transf. 150, 42–54. https://doi.org/10.1016/j.jqsrt.2014.06.023.